

This is an Open Access document downloaded from ORCA, Cardiff University's institutional repository: <https://orca.cardiff.ac.uk/id/eprint/118818/>

This is the author's version of a work that was submitted to / accepted for publication.

Citation for final published version:

Sanfilippo, A., Dick, H. J. B., Marschall, H. R., Lissenberg, C. J. and Urann, B. 2019. Emplacement and high-temperature evolution of gabbros of the 16.5°N oceanic core complexes (Mid-Atlantic Ridge): Insights into the compositional variability of the lower oceanic crust. *Geochemistry, Geophysics, Geosystems* 20 (1), pp. 46-66. [10.1029/2018GC007512](https://doi.org/10.1029/2018GC007512)

Publishers page: <http://dx.doi.org/10.1029/2018GC007512>

Please note:

Changes made as a result of publishing processes such as copy-editing, formatting and page numbers may not be reflected in this version. For the definitive version of this publication, please refer to the published source. You are advised to consult the publisher's version if you wish to cite this paper.

This version is being made available in accordance with publisher policies. See <http://orca.cf.ac.uk/policies.html> for usage policies. Copyright and moral rights for publications made available in ORCA are retained by the copyright holders.



1 **Emplacement and high-temperature evolution of gabbros of the**
2 **16.5 °N oceanic core complexes (Mid-Atlantic Ridge): insights into the**
3 **compositional variability of the lower oceanic crust**

4
5 **Sanfilippo A.^{1,2*}, Dick H.J.B.², Marschall H.R.^{2,3}, Lissenberg C.J.⁴, Urann, B.²**

6
7 1- Dipartimento di Scienze della Terra e dell'Ambiente - Università degli Studi di
8 Pavia, Via Ferrata 1, Pavia, Italy

9 2-Department of Geology and Geophysics - Woods Hole Oceanographic Institution,
10 Woods Hole, MA 02543, USA

11 3- Institut für Geowissenschaften, Goethe Universität Frankfurt, Altenhöferallee 1,
12 60438 Frankfurt am Main, Germany

13 4- School of Earth and Ocean Sciences, Cardiff University, Park Place, Cardiff CF10
14 3AT, UK

15
16

17 *Corresponding Author: Alessio Sanfilippo (alessio.sanfilippo@unipv.it)

18
19

20 **Key Points:**

- 21 • Lower crust at the 16.5°N region of the Mid-Atlantic Ridge has a bimodal
22 composition.
- 23 • Thermodynamic models show that this distribution is expected in regions where
24 small gabbroic bodies are intruded into mantle peridotites.
- 25 • Deformation related to detachment faulting commenced under high-temperature
26 conditions (>1000 °C) as recorded by ultramylonites
27

28 **ABSTRACT**

29

30 This study reports the composition of the oceanic crust from the 16.5°N region of the Mid-
31 Atlantic Ridge (MAR), a spreading ridge segment characterized by a complex detachment
32 fault system and three main oceanic core complexes (Southern, Central and Northern OCC).
33 Lithologies recovered from the core complexes include both greenschist facies and weathered
34 pillow basalt, diabase, peridotite and gabbro, while only weathered and fresh pillow basalt
35 was dredged from the rift valley floor. The gabbros are compositionally bimodal, with the
36 magmatic crust in the region formed by scattered intrusions of chemically primitive plutonic
37 rocks (i.e. dunites and troctolites), associated with evolved oxide-bearing gabbros. We use
38 thermodynamic models to infer that this distribution is expected in regions where small
39 gabbroic bodies are intruded into mantle peridotites. The occurrence of ephemeral magma
40 chambers located in the lithospheric mantle enables large proportions of the melt to be
41 erupted after relatively low degrees of fractionation. A large proportion of the dredged
42 gabbros reveal evidence for deformation at high-temperature conditions. In particular,
43 chemical changes in response to deformation and the occurrence of very high-temperature
44 ultramylonites (>1000 °C) suggest the deformation related to the oceanic detachment
45 commenced at near-solidus conditions. This event was likely associated with the expulsion of
46 interstitial, evolved magmas from the crystal mush, a mechanism that enhanced the formation
47 of disconnected oxide-gabbro seams or layers often associated with crystal-plastic fabrics in
48 the host gabbros. This granulite-grade event was soon followed by hydrothermal alteration
49 revealed by the formation of amphibole-rich veins at high-temperature conditions (~900°C).

50

51

52 **1. INTRODUCTION**

53 Detachment faults, first reported as low-angle normal faults at the MARK area of the MAR
54 (Dick et al., 1981, Karson and Dick, 1983), are common at slow-spreading ridges. These long-
55 lived faults terminate at the foot of the rift valley wall, and produce a smooth surface with
56 corrugations parallel to the rifting direction (Cann et al., 1997). They expose large sections of
57 lower oceanic crust and abyssal mantle, commonly termed “megamullions” or oceanic core
58 complexes (OCCs) (Cann et al., 1997; Tucholke et al., 1998). The detachment faults operate
59 for up to several million years and exhume lower crust and mantle rocks, which are
60 continuously accreted and emplaced into the rift mountains from beneath a volcanic carapace
61 (Dick et al., 2008). Detachment faulting can account for 60–100% of the plate separation in
62 some ridge sections and may dominate a region for several millions of years (Tucholke et al.
63 1998; Smith et al., 2006, 2008; Schroeder et al., 2007; Baines et al., 2008; Escartín et al., 2008;
64 MacLeod et al., 2009). In particular, Escartín et al. (2008) and Smith et al. (2008) estimated
65 that close to 50 % of the Mid-Atlantic Ridge (MAR) from 12.5°N and 35°N is characterized by
66 detachment faults, indicating that a substantial portion of the seafloor in the central portion of
67 the MAR may form by such asymmetric spreading. Recently, some investigators have
68 suggested the proportion of seafloor formed by detachment faulting could be even higher, if
69 more fault surfaces are hidden under basaltic rafted blocks (e.g., Reston and Ranero, 2011).
70 Detachment faulting is now known as a major mechanism of crustal accretion at slow-
71 spreading ridges (Smith et al., 2014; Parnell-Turner et al., 2018).

72 The nucleation and growth of detachment faults is dependent on many factors, including
73 rheological differences between gabbros and serpentinitized mantle peridotites, spreading rate,
74 and magma budget (e.g., Cannat et al., 2006; Ildefonse et al., 2007; Escartin et al., 2008). For
75 instance, numerical modeling suggests that detachment faults form at intermediate levels of
76 magma supply (e.g.: Cannat et al., 2006) at slow- and ultraslow-spreading ridges when the
77 ratio of magmatic accretion to tectonic extension (M) lies between 0.3 and 0.5 (Tucholke et
78 al., 2008; Olive et al., 2010; Hansen et al. 2011). This is consistent with the common
79 occurrence of gabbroic lithologies exposed along the fault surfaces at oceanic core complexes

80 (e.g.: Dick et al., 1981; 1991; Cann et al., 1997; Dick et al., 2000; Blackman et al., 2007;
81 2011; MacLeod et al., 2009). In addition, it is likely that the mechanics of detachment
82 faulting in amagmatic environments differs from magmatic ones, where the fault roots into a
83 significant crystal mush zone beneath the rift valley and synmagmatic deformation can
84 enhance fault longevity and control fault geometry (Dick et al., 2000; Natland and Dick,
85 2001).

86 OCCs offer a unique opportunity to unravel the composition of the lower crust of ridge
87 segments formed at slow spreading ridges, although these observations are pertinent to the
88 sections exposed through detachment faulting; to what extent these observations apply to the
89 lower oceanic crust at symmetrically-spreading segments is uncertain. The large
90 compositional variability of the gabbros at OCCs worldwide suggests that the lower crust in
91 these sections is not that of the classic Penrose model (Conference Participants, 1972). At the
92 660-km²-gabbro massif at Atlantis Bank on the SW Indian Ridge ((I)ODP Holes 735B,
93 1105A and U1473) most of the gabbros recovered by seafloor sampling and drilling (up to
94 1.5 km) are olivine-gabbros interspersed with highly evolved (oxide-bearing) gabbros,
95 representing crystallization from nothing close to a primary magmatic liquid (Dick et al.,
96 2000; MacLeod et al., 2017). In contrast, the 1.4 km deep Hole U1309D at the Atlantis
97 Massif OCC, another large OCC exposed along the Mid-Atlantic Ridge, contains a much
98 broader range of lithologies, with large amounts of primitive gabbros such as troctolite, many
99 gabbro sensu-stricto (olivine <5 vol.%) and subordinate oxide-gabbros (>2% oxide)
100 (Blackman 2006, 2010). Large amounts of troctolites and olivine gabbros also constitute the
101 isolated intrusions in mantle peridotites at the Kane Megamullion, a large detachment system
102 south of the Kane Fracture Zone in the Atlantic (Dick et al., 2008), which nonetheless differ
103 from the Atlantis Massif by the absence of olivine-free gabbro but show a high amount of
104 oxide gabbro. Finally, ODP Leg 209 drilled a series of holes from 14°43' to 15°44'N
105 straddling the 15°20' Fracture Zone, providing a view of the lithostratigraphy to the south of
106 the 16.5° N core complexes. Notably, gabbro is rare, and the lower crust has a “bimodal”
107 distribution similar to that of the Kane area, with large amounts of troctolite and dunite and

108 oxide gabbro and oxide gabbronorite the most abundant lithologies. As a whole, the
109 compositional variability of gabbros recovered at OCCs suggests a variable, complex crustal
110 architecture, which emphasizes the need to characterize the lower crust at ridge segments
111 formed at different magma supplies, ridge geometries and tectonics, as part of interpreting
112 crustal petrogenesis.

113 This study aims at exploring the architecture and the composition of the lower crust
114 exposed along the 16.5°N region of the MAR. This segment is characterized by a complex
115 detachment fault system developed in a magma-poor regime: unlike the thick gabbroic
116 sections exposed at the Atlantis massif and Atlantis Bank OCCs, oceanic core complexes
117 identified in the 16.5°N MAR region are formed by scattered gabbroic intrusions within a
118 partly serpentinized mantle (Cannat and Casey, 1995, Cannat et al. 1997. This region is
119 characterized by a strong lateral crustal heterogeneity and an active detachment faulting
120 system (Smith et al., 2014; Parnell-Turner et al. 2016). As such, the MAR 16.5°N is similar
121 to the Kane and the 15°20' Fracture Zones, and is an ideal case to explore the petrological
122 processes driving the formation of the lower crust in regions of low magma supply and active
123 detachment. Here we present microtextural observations, major element mineral
124 compositions and discuss the process of emplacement and early deformation histories of
125 these rocks. We use thermodynamic modeling to explore the cause of the bimodal
126 lithological variability of the lower crust in this region, proposing that a close relationship
127 between magma supply, eruption rate and deformation-driven melt extraction may explain
128 the lithological variability of the lower oceanic crust exposed through detachment faulting.

129 **2. THE 16.5 °N REGION OF THE MID-ATLANTIC RIDGE**

130 The study area is located between 16° and 17°N and exposes an ~120 km stretch of the
131 slow-spreading Mid-Atlantic ridge (Fig. 1). This region encompasses two spreading segments
132 that strike ~012°, perpendicular to the inferred spreading direction (DeMets et al., 2010). The
133 spreading axis is characterized by a well-developed neovolcanic zone and by a remarkably high
134 rate of teleseismic and hydrophone-recorded seismicity (Smith et al., 2003). The area has also
135 been identified as a region of active detachment faulting, mostly concentrated on the west side

136 of the axis (Escartin et al, 2008).

137 RV Knorr Cruise 210 Leg 5 conducted bathymetric, dredging and AUV surveys focused on
138 the neovolcanic zone and western rift mountains (see Smith et al., 2014; Parnell-Turner et al.,
139 2018). Based on the occurrence of corrugated surfaces, different core complexes were
140 identified: I) the Southern Core Complex (SCC), a classic, domed, detachment fault with a
141 slope of 13° and corrugation wavelengths between 400 and 1600 m; II); the Central Core
142 Complex (CCC), characterized by two distinctive ridge-parallel, linear ridges (East and West
143 Ridges, Fig. 1), interpreted to be the breakaways of detachment faults that underwent
144 significant rotation (Macleod et al., 2009; Smith et al., 2006; Smith et al., 2008; Parnell-Turner
145 et al. 2018); and III) The Northern Core Complex (NCC). Compared to the South and Central
146 complexes, where the detachment faults intersect the valley floor with a well-developed axial
147 volcanic ridge, the NCC is flanked by a deep axial rift valley, covered by lava flows, but
148 lacking a neovolcanic ridge. This feature suggests that the formation of the NCC was
149 accompanied by limited volcanic activity compared to the Southern Core Complex.

150 During the RV Knorr Cruise 210 Leg 5 dredging program, we sampled both the footwall of
151 the detachment faults and the volcanic rocks exposed on the associated ridge axis (72 dredges
152 in total). Overall, ~5,800 kg of basalt, diabase, gabbro (s.l.), and peridotite samples were
153 dredged in 63 locations (see Table S1 of the supplementary material). However, the proportions
154 of different rock types vary significantly across the area (Fig. 2). Pillow basalt is the most
155 abundant dredged lithology at all the three core complexes. They have been collected from
156 both the crests of the complexes (i.e. detachment breakaway zone) and as the hanging wall
157 debris resting on the detachment fault footwall. Mantle peridotites (harzburgites to dunites) are
158 abundant in the CCC, whereas only gabbroic rocks were collected at the NCC. A very limited
159 amount of gabbroic lithologies (~1 kg in total) were recovered at the southern and central core
160 complexes, limited to small intrusions within mantle peridotites. The main characteristics of
161 these areas are reported in Smith et al. (2014) and Parnell-Turner et al. (2018). Here we focus
162 our analyses on the NCC and its surrounding areas, capitalizing on the abundance of gabbroic
163 lithologies there to infer lower crustal formation and evolution.

164

165 **2.1. Northern core complex and its surroundings**

166 The gabbros we studied were mainly collected at the Northern Core Complex. This complex is
167 delineated by a detachment fault, which is locally masked by several rafted blocks of volcanic
168 crust. Smith et al. (2014) suggested that these blocks were produced by short-lived steep-
169 dipping normal faults formed close to the rift axis that merged at depth with the primary
170 detachment fault (see Reston and Ranero, 2011). Each fault block is covered by volcanic
171 hummocks and flows similar to those on the valley floor. The median valley adjacent to the
172 NCC is narrow (3–4 km) and deep (~4,500 m), and is characterized by smooth, likely
173 sedimented surfaces covering flat-topped lava flows and hummocks. Although there is no
174 neovolcanic axial ridge, the occurrence of volcanic ridges and hummocks emerging from the
175 sediments at the west side of the median valley and the flows on the rift valley floor suggest
176 that this segment was volcanically active in the recent past. Several dredges were deployed at
177 the central portion of the NCC, recovered 579 kg of fresh pillow basalts from the terrace of the
178 rafted block (D52, D56, D57, D65).

179 237 kg of gabbroic rocks were recovered in 10 of 14 dredge hauls (i.e., D49 to D55, D59,
180 D60, D63, D64, D67, D69, D70, D72) deployed along a ridge around the complex (from the
181 southern shoulder to two narrow ridges in the north). Gabbros in this locations are associated
182 with 157 kg of peridotite sampled in 8 dredges and 513 kg of fresh pillow basalts found in 6
183 dredges. Dredged gabbros were described macroscopically during the expedition. Each
184 member of the Shipboard Party was responsible for one or more aspects of the description (e.g.,
185 rock-type, textures, mineral modes and habits) to ensure consistency throughout the dredged
186 hauls. Only primary minerals were considered to define the initial modal proportion;
187 completely altered rocks are referred to as metagabbros (Table S1 of supplementary material).
188 Representative sample images are displayed in Figure 3. Preliminary onshore analyses followed
189 the shipboard observations in order to test the accuracy of the definition of rock types and
190 deformation intensity. Samples reviewed for the present study provided a good correspondence
191 with the shipboard observation, although minor interstitial phases such as orthopyroxene and

192 amphibole had been commonly underestimated (see textural description). This generally did
193 not affect the classification of the rock types, which is based on major mineral phases. The
194 proportions (wt.%) of different gabbroic rocks collected from each dredge are reported in
195 Figure 2, which shows that the lower crust exposed at NCC displays a bimodal distribution,
196 i.e., high proportions of primitive plutonic rocks (i.e., dunites and troctolites >60 wt.%)
197 associated with evolved gabbro-norites to oxide gabbros (~30 wt.%). Intermediate rocks such
198 as olivine gabbros (olivine >5 vol.%; clinopyroxene >10 vol.%; oxides <2 vol.%) and gabbros
199 *sensu strictu* (olivine <5 vol.%; oxides <2 vol.%) and gabbro-norite (olivine <5 vol.%;
200 orthopyroxene >5 vol.%) are very limited, as they are to the south. Interestingly, troctolites
201 were mainly collected in two dredges (D59, D60; Fig. 2) otherwise characterized by large
202 proportions of serpentinized dunites and pyroxene-bearing peridotites, and by the absence of
203 volcanics. The exposure of mantle peridotites, dunites and troctolites and rarity of basalts are
204 typical of sequences thought to represent crust-mantle transitions, such as the OPD Site 895 at
205 Hess Deep (Dick and Natland, 1996), the Adam Dome at the Kane FZ (Dick et al., 2008), the
206 breakaway area of the Godzilla Megamullion (Sanfilippo et al, 2013; 2016a), and the Uraniwa
207 Hills at the Central Indian Ridge (Sanfilippo et al., 2015; 2016b).

208

209 **3. MAIN PETROGRAPHIC FEATURES OF MAR 16.5° N GABBROS**

210 **3.1 Igneous textures**

211 Troctolites have euhedral to subhedral olivine and plagioclase, locally showing sub-rounded
212 grain boundaries and a poikilitic texture (Fig. 4a). Clinopyroxene commonly occurs as films or
213 discrete grains interstitial to olivine and plagioclase. Large clinopyroxene oikocrysts (up to 7
214 mm) are locally present within the olivine-plagioclase matrix, commonly including euhedral to
215 irregular plagioclase and olivine chadacrysts (Fig. 4b). Clinopyroxene oikocrysts show film-
216 like apophyses interstitial to olivine and plagioclase, locally associated with orthopyroxene
217 films. In a few cases, oikocrystic clinopyroxene reaches 10 vol.% of the rock, forming
218 spatially defined Ol-gabbro domains. Pargasitic brown amphibole is common within the
219 troctolites as films or interstitial discrete grains locally reaching 0.1 mm (Fig. 4c). One

220 troctolite contains large amphibole oikocrysts up to 3 mm. These oikocrysts include rounded
221 plagioclase chadacrysts, having irregular grain boundaries taken as evidence of partial
222 dissolution (Fig. 4d). Fe-Ti oxides are locally present in troctolites, but are restricted to within
223 the interstitial brown amphibole at the rim of olivine or plagioclase.

224 Gabbros and gabbronorites consist of plagioclase and pyroxenes commonly showing a
225 subophitic texture. Olivine is absent or restricted to small grains (<0.5 mm) rounded in shape.
226 Small (<0.1 mm) irregular grains of Ti-Fe oxides and apatite are locally included in the
227 pyroxenes or at the rim of pyroxene-plagioclase crystals. Orthopyroxene in gabbronorites
228 occurs in large, subequant crystals with subhedral habit, as distinguished from intergranular
229 rims commonly found in olivine gabbros. Pargasitic brown amphibole is rare in these rocks,
230 and present as <0.05 mm-thick films around clinopyroxene.

231 Oxide gabbros (>2% oxide) have been found as i) coarse (up to 20 cm) grained massive
232 samples and as ii) medium/fine-grained centimeter-sized seams crosscutting either gabbros or
233 gabbronorites. In both cases, oxide gabbros are mostly constituted by granular plagioclase,
234 clinopyroxene and locally orthopyroxene, and abundant (up to 15 vol.%) Ti-Fe oxides. Olivine
235 is absent from all of these rocks, whereas accessory phases such as zircon and apatite are
236 commonly present. Brown pargasitic amphibole is ubiquitous within the oxide gabbros,
237 occurring as interstitial grains to coronas surrounding opaque minerals or as blebs within partly
238 exsolved clinopyroxene. Coarse-grained oxide gabbros contain irregular oxide-rich patches up
239 to 10 mm wide separating, and in some cases, surrounding aggregates of disrupted plagioclase
240 and clinopyroxene grains. The oxide-rich domains locally include small plagioclase and/or
241 apatite grains (0.1-0.5 mm), subhedral to rounded in shape. The oxide-gabbro seams are
242 typically found as medium to fine-grained, centimeter-sized layers parallel to the foliation in
243 the host rock. They have a planar aspect and well-defined sutured contacts with the host
244 gabbros, although oxide minerals can be locally dispersed in the host rock a few millimeters
245 from the contact.

246

247 **3.2 Textures indicative of high-temperature deformation**

248 Metamorphic grade and crystal-plastic fabric intensity were documented for each sample,
249 which were cut perpendicular to the foliation where possible. Approximately 40% of the
250 gabbros preserve textures indicative of shearing and recrystallization under hyper- to
251 subsolidus conditions. Deformation intensity was classified on a scale from 0 to 5 (0,
252 undeformed; 1, slightly deformed; 2, sheared; 3, protomylonitic; 4, mylonitic and 5,
253 ultramylonitic) based on the foliation, grain size and relative proportions of neoblasts and
254 porphyroclasts. The distribution of the deformation intensity for the different rock-types (Fig.
255 5) suggests that the higher grade crystal-plastic deformation (grades 3 to 5) is equally recorded
256 by primitive and evolved gabbros, while oxide gabbros and gabbro-norites seem to be on
257 average more deformed than troctolites (~50% and ~30% of the total, respectively) at lower
258 grades.

259 *3.2.1-Granulite grade deformation*

260 Protomylonites and mylonites generally appear to be indistinguishable on the basis of mineral
261 proportions from their protoliths, which is not the case for ultramylonites (Fig. 6a; b).
262 Protomylonites are defined by the occurrence of a porphyroclastic texture that locally grades
263 into mylonites having alternating bands of neoblastic plagioclase, olivine and/or
264 clinopyroxene (Fig. 3). The mylonitic zones are up to decimeter wide, although we cannot
265 determinate the original thickness because undeformed portions of the same rock are not
266 recovered. The most common metamorphic assemblage includes recrystallized olivine,
267 pyroxenes and plagioclase. Depending on the protolith, spinel (in troctolites) or Ti-Fe oxides
268 (in gabbros and oxide gabbros) are also found as neoblastic phases. Olivine, pyroxenes and
269 plagioclase porphyroclasts are kinked, folded, and displaced by subgrain boundaries. Equant
270 to subequant neoblasts surround porphyroclasts of the same mineral, suggesting subgrain
271 boundary rotation and recrystallization under high-temperature conditions (Miranda and
272 John, 2010; Hansen et al., 2013). Trace amounts of pargasitic amphibole are locally found
273 within the neoblastic assemblage, as small (<0.1 mm) grains in textural equilibrium with the
274 major phases. Samples showing this metamorphic assemblage will be referred to hereafter as

275 “gabbro granulites”, in analogy with the definition of similar rocks from other oceanic core
276 complexes worldwide (see Dick et al., 2000; Blackman et al., 2006; 2011; Ildefonse et al.,
277 2007; Dick et al., 2008; Miranda and John, 2010; Hansen et al., 2013; MacLeod et al., 2017).

278 3.2.2-Ultramylonites

279 The mylonites locally grade into 5 to 10-mm thick, very fine-grained (<0.1 mm) ultramylonitic
280 bands. These bands are always found in the median portions of the mylonites, and have sub-
281 planar shape and sharp boundaries towards the host rock (Fig. 3). Unlike the mylonites, which
282 are mineralogically indistinguishable from the magmatic protolith, the ultramylonites have a
283 distinct mineralogical composition. We found ultramylonites developed from different
284 protoliths ranging from troctolites (Fig. 6a) to oxide gabbros (Fig. 6b). These two end-
285 members will be described hereafter.

286 *i)* Figure 6a shows a ~5-mm thick ultramylonite located within a troctolite mylonite. The host
287 protomylonite and the mylonite are formed by olivine and plagioclase porphyroclasts
288 mantled by a neoblastic assemblage of plagioclase and olivine, locally including
289 clinopyroxene and brown amphibole (Ti-pargasite). Spinel porphyroclasts are also present
290 and partly recrystallized along the main foliation planes. In contrast, olivine and spinel are
291 absent in the ultramylonite band, which is mainly formed by a very fine-grained (<0.1 mm)
292 assemblage of plagioclase and brown amphibole (Ti-pargasite) and rare clinopyroxene.
293 Both clinopyroxene and brown amphibole are locally replaced by green amphibole and
294 chlorite in a coronitic texture.

295 *ii)* Figure 6b shows an up to ~5-mm thick ultramylonite band located within an oxide-gabbro
296 mylonite. The host mylonite is characterized by plagioclase and clinopyroxene
297 porphyroclasts immersed in a neoblastic assemblage of plagioclase, clinopyroxene and Ti-
298 Fe oxides (~5-10 vol.%). Pale to green amphibole (hornblende) statically replacing the
299 neoblastic clinopyroxene is abundant, whereas brown amphibole is absent. In contrast, the
300 ultramylonite band is characterized by a very fine-grained assemblage of plagioclase and
301 brown amphibole (Ti-pargasite) locally associated with minor clinopyroxene, and by the
302 absence Ti-Fe oxides. Similar to the ultramylonite located in the troctolite, green

303 amphibole and chlorite locally replace the brown amphibole and the clinopyroxene.
304 Taken as a whole, despite the fact that the two ultramylonites developed from different
305 magmatic protoliths, the ultramylonites are texturally and mineralogically indistinguishable,
306 consisting of a fine-grained neoblastic assemblage of plagioclase, brown amphibole and, more
307 rarely, clinopyroxene.

308

309 **3.3 Textures indicative of high-temperature alteration**

310 Deformed gabbros locally show traces of alteration at high-temperature conditions
311 (amphibolite facies). This process is mainly indicated by *i*) the occurrence of amphibole-rich
312 veins crosscutting the foliation in the host gabbros at high angle; *ii*) the occurrence of pale-
313 brown amphibole (hornblende) statically replacing the clinopyroxene. These textures are
314 well exemplified in Figure 3e3f, which shows a sheared gabbro crosscut by an
315 undeformed amphibole-rich vein, at high angle with the main foliation in the host rock.
316 Hornblende in the veins shows a fibrous texture and is elongated parallel to the vein wall.
317 Plagioclase close to the contact with the vein is statically recrystallized in a fine-grained
318 assemblage. Clinopyroxene in the host gabbro is almost totally replaced by single grains or
319 aggregates of hornblende spatially locally associated with very fine-grained (<0.05 mm)
320 albitic plagioclase (Fig. 3f). Similar textures are also found where irregular veins crosscut the
321 gabbros, leading to the formation of hornblende at the expense of clinopyroxene, and fine-
322 grained plagioclase replacing the coarse plagioclase of magmatic origin. In almost all of the
323 samples, hornblende is locally rimmed or partially replaced by green amphibole and chlorite,
324 as a response to lower-temperature greenschist facies alteration.

325

326 **4. MAJOR ELEMENT MINERAL COMPOSITIONS**

327 Major element mineral compositions of selected 16.5°N gabbros were obtained using a JEOL
328 JXA-8200 electron microprobe (Dipartimento di Scienze della Terra, Università degli Studi di
329 Milano, Italy) at 15 kV accelerating voltage and 15 nA beam current. Counting time was 30 s
330 on the peak and 10 s on the backgrounds. Natural silicates were utilized as standards and data

331 reduction was carried out using the CITZAF package (Armstrong 1995). Undeformed and
332 variably deformed samples ranging from troctolites to oxide gabbros were selected for the
333 microprobe study, in order to cover the main chemical variability of the rock-types.
334 Representative analyses of olivine, plagioclase, pyroxene and amphibole of selected samples
335 are reported in supplementary material in Tables S2 to S6. Four samples were also mapped
336 using a Zeiss Sigma HD field emission gun SEM installed at Cardiff University. This machine
337 is equipped with dual 150-mm² Oxford Instruments X-Max^N energy dispersive silicon drift
338 detectors, which enable high count rates (>1,000,000 cps) to be obtained. The data were
339 background corrected using Oxford Instruments AZtec software prior to the production of
340 element maps.

341 Olivine in troctolites has high forsterite (Fo) contents (86 to 88 mol.%), and relatively
342 constant NiO (0.20–0.25 wt.%) and MnO (0.19–0.25 wt.%) contents. There is no
343 compositional difference between porphyroclastic and neoblastic olivine. Plagioclase anorthite
344 content varies from An₈₁ in troctolites to An₄₆ in oxide gabbros. Chemical analyses and
345 element maps clearly show that high-temperature deformation is associated with a decrease in
346 anorthite in plagioclase neoblasts compared to porphyroclasts in the same rock. This is well
347 illustrated in Figure 7a, where compositional maps for Na contents of a sheared troctolite are
348 shown. In particular, the lower Na (and higher Ca, not shown) of the fine-grained neoblasts
349 clearly indicates lower An contents (~78 mol.%) compared to that of the porphyroclasts (~81
350 mol.%). Similarly, an even greater variation in plagioclase anorthite component characterizes
351 the troctolite mylonite–ultramylonite association (Fig. 7b). Here, the plagioclase in the
352 ultramylonite has lower Ca (and higher Na) compared to that in the mylonite, resulting in a
353 decrease from An₈₁ in the mylonites to An₆₅ in the ultramylonite. A unique exception is
354 represented by the mylonite–ultramylonite association in the oxide gabbro-norite (Fig. 7c),
355 where compositional maps show higher Ca and lower Na contents of the plagioclase in the
356 ultramylonite (An₈₂) compared to that in the host mylonite (46 mol.%). Finally, a decrease in
357 anorthite component is apparent in recrystallized plagioclase associated with the formation of
358 the amphibole-rich vein in Figure 7d. Here, the neoblastic plagioclase at the Amphibole-

359 vein/gabbro contact and the plagioclase in the vein has higher Na and lower Ca compared to the
360 plagioclase porphyroclasts, resulting in An_{53} for the former and $\sim An_{58}$ for the latter. Note that
361 very high Na and low Ca characterize the fine-grained plagioclase associated with veins and
362 microcracks crosscutting the magmatic phases (An_{20} to An_{25}).

363 Clinopyroxene shows a wide compositional range with Mg# ($100 * Mg / \{Mg + Fe\}$)
364 varying from 89 in oikocrystic clinopyroxene in troctolites to 65 in oxide gabbros.
365 Clinopyroxene in troctolites is distinct from that in gabbros by generally higher Cr_2O_3 and
366 Al_2O_3 contents (0.4–1.5 wt.% compared to <0.2 wt.% in the gabbros), but high TiO_2 contents
367 (Fig. 8). Chemical mapping suggests that clinopyroxene neoblasts in sheared to mylonitic
368 rocks are nearly indistinguishable from the porphyroclasts in the same sample. The only
369 exception is the clinopyroxene in oxide gabbro mylonites/ultramylonite shown in Figure 7c,
370 which has a sharp change in chemical composition from the mylonite (Mg#=64–67;
371 $Cr_2O_3=0.01–0.02$ wt.%) to the ultramylonite (Mg#=73; $Cr_2O_3=0.5$ wt.%). With the exception
372 of this ultramylonite, there is a positive correlation between Mg# in clinopyroxene and
373 anorthite content in coexisting plagioclase from each sample (Fig. 9a).

374 Orthopyroxene Mg# is well correlated with Mg# of coexisting clinopyroxene (Fig. 9b).
375 Similar to clinopyroxene, orthopyroxene from our sample suite is characterized by (i) high Mg#
376 and Cr_2O_3 contents (87–89; 0.4–0.6 wt.%, respectively) in troctolites and progressively lower
377 (75–58; 0.01–0.04 wt.%) in gabbro/gabbronorite/oxide gabbro, and (ii) lack of correlation
378 between TiO_2 and Mg#. The composition of the coronitic to interstitial orthopyroxene in the
379 troctolites suggest a magmatic rather than a metamorphic origin, similar to the granular
380 orthopyroxene in the gabbronorites.

381 Amphibole is a ubiquitous phase in our samples. There is a clear chemical distinction
382 between the green to pale-brown amphibole statically replacing clinopyroxene (Type I) and the
383 brown amphibole forming poikilitic to interstitial grains in undeformed samples or found as
384 neoblasts within the granulites (Type II; Fig. 10). Type I amphibole occurs in two forms: i)
385 green amphibole with very low Al^{IV} (<0.39 atoms per formula unit, apfu), TiO_2 (<0.41 wt.%)
386 and alkalis [(K+Na)<0.12 atoms per formula unit, apfu], mainly consisting in actinolite and

387 tremolite (Fig. 10); ii) pale-brown amphibole, having higher Al^{IV} (0.83–1.29 apfu), TiO_2 (0.3–
388 1.4 wt.%) and alkalis (0.49–0.78 apfu) and mostly represented by hornblende (Fig. 10b). Pale-
389 brown hornblende also constitutes the amphibole-rich veins. These amphiboles have Al^{IV}
390 (1.24–1.41 apfu) and alkalis (0.51–0.82 apfu) partly overlapping those in the amphibole
391 coronas, but have higher TiO_2 contents (3.0–3.3 wt.%). TiO_2 contents of the hornblende in the
392 vein decrease towards the rim. Chlorine in hornblende coronas and hornblende in veins varies
393 between 0.1–0.2 wt.% (Fig. 10b, c).

394 In contrast, Type II amphibole is brown to reddish brown, and mostly consists of Ti-
395 pargasite. Within the undeformed troctolite and gabbro samples, this amphibole has high Al^{IV}
396 (1.74–1.82 apfu) and alkalis (0.61–0.79 apfu) and very high TiO_2 contents (4.2–4.9 wt.%) and
397 high Mg# (Fig 10d). Chlorine is lower than the detection limit of the microprobe analyses (~
398 0.1 wt.%) (Fig. 10b, c). Similar to the hornblende in the amphibole veins crosscutting the
399 gabbros, the large amphibole oikocryst in troctolites show a sharp decrease in Al^{IV} and TiO_2
400 from the core towards the rim. Amphibole neoblasts in mylonites and ultramylonites are
401 chemically similar to the magmatic amphibole in undeformed samples. They have high Al^{IV}
402 (1.50–1.82 apfu) and alkalis (0.62–1.80 apfu), low chlorine (<0.1 wt.%), and highly variable
403 TiO_2 contents (1.5 to 4 wt.%). The neoblastic amphiboles in the two ultramylonites are overall
404 similar to both the magmatic amphibole and the neoblastic amphibole in the mylonite. The
405 amphibole in the troctolitic ultramylonite tends to have higher Al^{IV} and TiO_2 contents and Mg#
406 than the amphibole in the oxide gabbro ultramylonite (Fig. 10b; d).

407 5. DISCUSSION

408 5.1-Bimodal distribution of gabbros from the 16.5° N region of Mid-Atlantic Ridge: a 409 quantitative model to explain the compositional variability of the lower oceanic crust

410 The composition of the gabbroic rocks collected from the 16.5° N region of the MAR
411 indicates a lower oceanic crust most likely formed by scattered intrusions of chemically
412 primitive gabbros (i.e. troctolites), mainly associated with evolved gabbro-norites and oxide-rich
413 gabbros. Intermediate rocks such as olivine-gabbros and gabbro *sensu stricto* are restricted to
414 <3 wt.% of the ~356 kg of gabbros sampled in the region (Fig. 2). This bimodal distribution is

415 remarkably different to that of the gabbroic section drilled at Hole U1309D (Blackman et al.,
416 2006; 2011), formed in a relatively robust magmatic center along the Mid-Atlantic Ridge
417 (Godard et al., 2009). It also contrasts sharply with the Atlantis Bank gabbro massif on the SW
418 Indian Ridge, which is dominated by moderately fractionated olivine gabbro that grades into
419 subordinate highly evolved oxide gabbros (e.g.: Dick et al., 2000; MacLeod et al., 2017).

420 Motivated by the similarity of the gabbros exposed in the 16.5°N region with those of the Kane
421 Megamullion and in the vicinity of the 15°20' Fracture Zone, hereafter we examine how magma
422 supply and melt extraction may control the overall composition of the crustal sections exposed
423 through detachment faulting. We calculate the relative amount of different gabbroic lithologies
424 (i.e. dunites, troctolites, olivine gabbros, gabbros and oxide gabbros) crystallized during a
425 fractional crystallization process using the thermodynamic program *MELTS* (Ghiorso and
426 Sacks, 1998; Ghiorso et al., 2002). In order to take into account that part of the initial liquid
427 mass is erupted as basalt on the seafloor, we performed this calculation in different steps,
428 allowing a proportion of the liquid to be subtracted at each step of the crystallization process
429 (parameters and results of the model in Tables S7, S8, S9 of the supplementary files). The
430 starting liquid (*Liq 0*) is a primary melt formed by ~10 % melting of a DMM peridotite source
431 (Mg# ~72; Kinzler and Grove, 1993). After a defined amount of differentiation (for the sake of
432 simplicity fixed at $\Delta\text{Mg\#} \sim 4$), a precise mass of liquid (*Liq 1*) is subtracted and the remaining
433 composition of *Liq 1* is used as initial composition for the next step of differentiation. The
434 mass of liquid subtracted is calculated by scaling the melt mass in proportion to the
435 compositional distribution of the erupted basalts, which is thereby a fundamental input of our
436 model. We cannot use the observed compositional variability of basalts sampled exclusively in
437 the 16.5°N region, considering that the genetic relationships between the basalts along axis and
438 the gabbros exposed through detachment faulting is not obvious and that basalt sampling is
439 inevitably fragmentary. It has been previously noted that the compositional distribution of
440 basalts at the MOR is globally dependent on the spreading rates (Melson et al., 1976; Sinton
441 and Detrick, 1992). In particular, basalts erupted at slower-spreading ridges tend to be more
442 primitive compared to those erupted at fast-spreading ridges (Fig. 11). The large-scale

443 compositional variability of the basalts can thereby be considered meaningful, and allows us to
444 compare the results of our model with different lower crustal sections exposed along the same
445 ridge segment. Here, we used the overall compositional distribution of the basalts erupted along
446 the 10–35°N segment of the MAR, which comprises ~2,700 glass analyses selected from the
447 PetDB database (reference Lehnert paper), making the necessary assumption that the
448 distribution is constant for all the modeled scenarios. An explanation of the model is reported in
449 Figure 12.

450 The solid composition is calculated at each step from the total mass of crystallizing
451 phases given by the program (Fig. 13a; b). The crystallizing phases are restricted to olivine,
452 plagioclase, clinopyroxene and Fe-Ti oxide, following the fractionation trends inferred for a
453 MORB melt (see Grove et al., 1993). Minor phases such as orthopyroxene and amphibole are
454 not considered in the model because they occur as interstitial phases, likely related to
455 crystallization from intercumulus melt. This is in contrast to the primitive orthopyroxene-
456 bearing cumulates that have been sampled in different locations along the mid-ocean ridge
457 system. The orthopyroxene from these rocks has primitive compositions and may represent
458 crystallization from melts more depleted than typical MORB (e.g., Ross and Elthon 1995) either
459 derived from melting an hydrated mantle (Nonnotte et al. 2005) or from melt residual by
460 interaction with mantle peridotites (see also discussion in Gillis et al. 2014). However, it should
461 be noted that gabbro-norites having granular orthopyroxene as a cumulus phase were rarely
462 sampled in this study, and that these rocks do not contain olivine and have relatively evolved
463 mineral compositions, plotting in the field of the orthopyroxene-free gabbros (Figs 8 and 9).
464 For the sake of simplicity, we hence grouped the gabbro-norites with the gabbros *sensu stricto*
465 in our model. The total mass of initial liquid subtracted by eruption (M_e) with respect to that
466 crystallized (M_c) is referred to as M_e/M_c . At $M_e/M_c = 0$ the melt is totally retained in the lower
467 crust and the mass of gabbro crystallized corresponds to that of pure fractional crystallization.
468 At high M_e/M_c the melt is preferentially erupted and the relative mass of crystallized gabbros
469 decreases.

470 The proportion (mass %) of gabbros crystallized at different M_e/M_c (0 to ~7:3) is

471 shown in Figure 13, where the chemical and modal compositions of the crystallizing
472 assemblages and the distribution of the resulting erupted basalts are shown at steps of $\Delta Mg\#$ 4.
473 Remarkably, the olivine and clinopyroxene crystallized from the computed melt fits the
474 composition of the natural samples from this study very well. As was expected, this model
475 shows that at increasing M_c/M_c , a large proportion of the melt is erupted on the seafloor during
476 the first phase of crystallization. Hence, the crystallizing assemblage tends to be progressively
477 more primitive, i.e.: olivine \pm plagioclase assemblages are preferentially formed until the melt
478 is exhausted (Fig. 13e). At the same time, at high M_c/M_c ratios most of erupted melts are
479 restricted to basalts with very primitive compositions.

480 This simple scenario is highly improbable, however, as it implies that the liquid mass
481 is entirely extracted from the cumulate at each step of differentiation. Studies of oceanic
482 gabbros indicate that variable amounts of interstitial melt are retained within the crystal mush
483 (e.g.: Meyer et al., 1989; Natland and Dick, 2001). Hence, we assume that a proportion of
484 the initial melt is retained at each step of the crystallization process, following a separate
485 liquid line of descent (see Fig. 12). We must consider that the interstitial melts can crystallize
486 within the cumulus matrix at the closure of the magmatic system (e.g.: Tribuzio et al., 2000;
487 Borghini and Rampone, 2007) or can migrate through the crystal mush driven by buoyancy
488 differences or by compaction (e.g.: Dick et al., 2000; Natland and Dick, 2001). In both cases,
489 textural and geochemical evidence in gabbros suggest that these melts tend to partly
490 assimilate the crystal matrix, causing geochemical modification ascribable to assimilation–
491 fractional-crystallization (AFC) processes (e.g.: Coogan et al., 2000; Borghini and Rampone,
492 2007; Gao et al., 2007; Lissenberg and Dick, 2008; Drouin et al., 2009; Sanfilippo et al.,
493 2013; Lissenberg and MacLeod, 2016). The chemical response to these processes has been
494 modelled following equations from DePaolo (1981). These equations replicate the variations
495 in trace element compositions of the reacting melts and of the phases crystallized from it (see
496 Coogan et al., 2000; Gao et al., 2007; Borghini and Rampone, 2007; Lissenberg et al., 2013;
497 Sanfilippo et al., 2015; Lissenberg and MacLeod, 2016). They have been successfully used to
498 test AFC hypotheses in well-constrained melt-rock reaction scenarios, such as the conversion

499 of dunite to troctolite (e.g., Rampone et al., 2016 and reference therein) or troctolite to
500 olivine-gabbro (Lissenberg and Dick, 2008). When applied to the scale of the entire oceanic
501 crust, a process of assimilation would introduce a number of independent variables (i.e., the
502 modal amount of mineral phases involved; the chemical compositions of the reactants; the
503 mass assimilate/mass crystallized ratios; see discussion in Lissenberg et al., 2013). Such a
504 model could not be reproduced by the *MELT* model used here.

505 As a simplification, at each step we subtracted a certain amount of melt proportional
506 to the melt density (Fig. 13d), considering that a maximum of 30% of liquid can initially be
507 trapped in the solid framework before migrating upwards due to compaction by density
508 driven flow (Morse, 1979; Meyer et al., 1989). Then we calculate the gabbros crystallized
509 from the total mass of trapped melts (Fig. 12). The mass of gabbro resulting from this
510 calculation was then added to that of the gabbros previously obtained. Note that owing to an
511 increase in melt density with the chemical evolution, our model supposes that the amount of
512 melt potentially trapped in the crystal framework increases at decreasing liquid Mg#. This
513 causes a dependence of the amount of trapped melt on the M_e/M_c ratio, with a more extensive
514 melt entrapment occurring at low M_e/M_c ratios (Fig. 13e).

515 As expected, this calculation shows that the relative amount of evolved lithologies
516 (mainly oxide-gabbro) increases in all the modelled scenarios (Fig. 13e). In particular, at high
517 M_e/M_c ratios, most of the initial liquid is erupted on the seafloor before the melts reach
518 saturation in clinopyroxene, thereby preventing the formation of moderately evolved gabbros
519 (olivine-gabbros and gabbros *sensu stricto*). However, at the same time, the occurrence of
520 trapped liquid enables the local formation of evolved lithologies as this melt migrates due to
521 upward compaction and lateral density driven flow (gabbro-norites to oxide gabbros). As a
522 consequence, at high M_e/M_c ratios the model is able to produce a bimodal distribution of the
523 gabbros, characterized by large proportions of primitive lithologies and lack of intermediate
524 compositions.

525 It is noteworthy, however, that the model fails to reproduce the large amount of oxide
526 gabbros present in the 16.5 °N region. There are several factors that can account for this. Most

527 oxide gabbros appear to be formed by interstitial melts expelled from the cumulate matrix and
528 by upward compaction and/or high temperature deformation into narrow zones of the crystal
529 mush often associated with shear zones along the detachment fault surface (Dick et al., 2000;
530 Natland and Dick, 2001; Macleod et al., 2017). Moreover, it has been recently observed that in
531 addition to an upward increase in oxide gabbros at the Atlantis Bank gabbro massif, that the
532 body is laterally zoned to more evolved cumulates that comprise the entire section from the
533 base of the crust to the dike-gabbro transition at the distal end of the body near the bounding
534 Atlantis II Transform (MacLeod et al., 2017). This shows that density driven lateral flow by
535 either direct intrusion or permeable flow plays a major role in the architecture of the lower
536 oceanic crust. Thus, as seen at the Kane Megamullion (Dick et al., 2008) and Atlantis Bank
537 (MacLeod et al., 2017), while dunite and troctolitic dikes are rare in mantle massifs adjacent to
538 major magmatic centers at slow spreading ridges, oxide gabbro dikes are widely distributed
539 lithology. Thus, the amount of oxide gabbros can be biased by dredging and drilling in areas of
540 low magma flux, with highly centralized magmatic centers and intervening relatively
541 amagmatic regions, as from 13° to 17°N on the MAR (e.g.: Mendel et al., 1997, Sauter et al.,
542 2001, Standish et al., 2008). Finally, we emphasize that any AFC process would tend to
543 increase the incompatible element composition of the interstitial melt (see Lissenberg and
544 MacLeod, 2016 and reference therein), producing melts anomalously enriched in incompatible
545 elements compared to a melt evolving through fractional crystallization. This suggests that a
546 melt produced by AFC would potentially enriched the melt in Ti, bringing the saturation in Fe-
547 Ti oxides forward, and producing higher amounts of oxide-bearing lithologies. This is another
548 possible reason why our model seems to underestimate the amount of oxide-gabbros compared
549 to the natural occurrences.

550 Although fairly simplistic, in combination with insight provided by field mapping into
551 ocean crust architecture, this model provides insight into why a bimodal distribution of the
552 lower oceanic crust may be expected in regions where a high proportion of liquid produced in
553 the mantle is erupted on the seafloor, with a minor proportion of intrusive rocks. This scenario
554 recalls the “plum-pudding model” suggested for slow-spreading ridges (Cannat, 1993, Cannat

555 et al., 1995; 1997), which proposes that the lower oceanic crust might consist of small gabbroic
556 plutons scattered within the lithospheric mantle (see also Kelemen et al., 2004; Dick et al.
557 2008; 2010).

558 The outcomes of our model are consistent with the compositional heterogeneity of the
559 lower oceanic crust along the MAR (Fig. 13). For instance, a lower oceanic crust mainly
560 consisting of primitive gabbros and highly evolved lithologies is expected at regions
561 characterized by scattered injections intruded within mantle peridotites, such as the region
562 considered here or the 15°20'N fracture zone drilled during Leg 209 (Kelemen et al., 2004).
563 On the other hand, a lower oceanic crust mostly composed of moderately evolved gabbros
564 associated with primitive lithologies (troctolites and dunites) and minor oxide gabbro is
565 expected in areas of a thick crust and moderate melt supply. This can be the case for relatively
566 robust magmatic segments as for instance the Atlantis Massif OCC (Blackman et al., 2007;
567 2011; Ildefonse et al., 2007; Godard et al., 2009; Drouin et al., 2009; 2010) or the crustal
568 transect exposed at the Adam Dome of the Kane megamullion (Dick et al., 2008) (Fig. 12d).

569

570 **5.2 Emplacement and crystal-plastic deformation of the NCC gabbros**

571 Clinopyroxene in the 16°30'N gabbros are characterized by different combinations of
572 Mg# and TiO₂ contents (Fig. 8). In particular, they show two distinct chemical trends in
573 troctolites (Trend 1) and gabbros/gabbronorites/oxide gabbros (Trend 2). The
574 clinopyroxenes following Trend 1 show a sharp increase in TiO₂ at nearly constant Mg#;
575 whereas those following Trend 2 display a gradual increase in TiO₂ at decreasing Mg#
576 followed by (from Mg# ~70) a renewed decrease in TiO₂. These chemical trends are typical
577 for clinopyroxene from abyssal gabbros (see Coogan, 2007) and respectively explained as
578 (Trend 1) evidence for magmatic metasomatism (i.e., melt–rock reactions) in a troctolitic
579 matrix (see also Lissenberg and Dick, 2008; Suhr et al., 2008; Drouin et al., 2009; Sanfilippo
580 and Tribuzio, 2013; Sanfilippo et al., 2013; 2015a; b; Lissenberg and MacLeod, 2016);
581 (Trend 2) evidence for progressive magmatic differentiation followed by saturation in Fe-Ti
582 oxides to form the oxide gabbros. The gradual decrease in clinopyroxene Mg# versus

583 plagioclase An contents, and the variability of the Cpx suggest that the
584 troctolite/gabbro/oxide-gabbro series crystallized from cogenetic melts evolving through
585 fractionation of Ol, Pl, Cpx and, finally, Ti-Fe oxides. Despite this, it seems obvious that the
586 crystallization of Cpx in the troctolites also involved interactions between the olivine and
587 plagioclase matrix and an evolved interstitial melts. This is consistent with the occurrence of
588 large brown amphibole occurring as interstitial to oikocrystic grains within the troctolites
589 (Fig. 4c;d). This amphibole locally shows poikilitic textures with inclusions of irregular
590 plagioclase chadacryst and small Ti-Fe oxides, and is characterized by high TiO₂, (K+Na)
591 and Al, and negligible Cl contents (Fig. 10). The poikilitic texture and the chemical
592 compositions are reconcilable with a magmatic origin, indicating the crystallization of late-
593 stage melts enriched in water and incompatible elements (see also Tribuzio et al., 2000;
594 Coogan et al., 2001; Borghini and Rampone, 2007). Hence, in agreement with the extensive
595 literature data for abyssal gabbros (e.g., Lissenberg et al., 2008; Suhr et al., 2008; Drouin et
596 al., 2009; Renna and Tribuzio, 2010; Sanfilippo et al., 2013; 2015; Lissenberg and MacLeod,
597 2016; Rampone et al., 2016), the enrichments in TiO₂ in the high-Mg# clinopyroxene and the
598 occurrence of magmatic amphibole with poikilitic texture testify that the 16.5°N troctolites
599 underwent a process of magmatic metasomatism by an interstitial, evolved melt. Below, we
600 show that evolved melts were also locally present at the onset of the deformation related to
601 the detachment faulting.

602 A large proportion of the 16.5°N gabbros show textures associated with a process of
603 deformation under high-temperature conditions (Fig. 3). In particular, most samples have
604 olivine, plagioclase, and clinopyroxene recrystallized in polygonal aggregates that are often
605 associated with brown amphibole and Ti-Fe oxides. The amphibole neoblasts in all deformed
606 troctolites (sheared, mylonites, and ultramylonites) are compositionally identical to the
607 magmatic amphibole in the undeformed samples. In addition, the occurrence of deformed
608 amphibole porphyroclasts in a sheared troctolite and the textural equilibrium with the other
609 neoblastic phases (olivine, plagioclase and clinopyroxene) clearly indicate that the formation
610 of paragonitic amphibole in this sample predated the “anhydrous” granulite-facies deformation

611 event.

612 The edenite-richterite amphibole-plagioclase thermometer of Holland and Blundy
613 (1994) on adjacent grains of amphibole and plagioclase was selected to infer the temperature
614 of recrystallization (Fig. 14). In one mylonitic troctolite, the amphibole-plagioclase
615 thermometry was also confirmed by two-pyroxene thermometry (Lindsley and Frost, 1992),
616 which yielded similar temperature estimates (see Fig. 14). Independent of rock-type, the
617 amphibole-plagioclase thermometer provided high temperature estimates for the granulite-
618 grade deformation, varying between 930 °C and ~1010 °C. These estimates fall in the range
619 of temperature estimated by Mehl and Hirth (2008), who showed that granulite-facies
620 deformation in gabbros from Hole 735B occurred at temperatures as high as 946 ± 70 °C.
621 These data suggest that the crystal-plastic deformation, which caused dynamic
622 recrystallization and formation of neoblasts of olivine + clinopyroxene ± brown amphibole in
623 the troctolites took place at hyper-solidus conditions (close to the solidus temperature of the
624 magmatic system). The high equilibration temperatures (1004 ± 20 °C; Fig. 14) estimated on
625 the basis of the coexistence of clinopyroxene–orthopyroxene in one troctolite mylonite
626 confirm this hypothesis. We must note that these temperatures are very close to the stability
627 limit of pargasitic amphibole at low pressures, which is considered to be at temperatures
628 <1000 °C (Koepke et al., 2004; 2005; 2007). Hence, one possibility is that the temperature
629 estimates for the mylonites give the crystallization temperature of an amphibole formed by a
630 melt present during the deformation process. The chemical modifications in the neoblastic
631 plagioclase of the sheared troctolite in Figure 7a, which has lower anorthite compared to that
632 of the porphyroclasts (An_{78} and An_{81} respectively) may also suggests that the granulite facies
633 deformation in the mylonites might have occurred in the presence of interstitial melt.

634 Although this idea would need to be better constrained by a more thorough chemical
635 characterization of the porphyroclastic and neoblastic minerals in the mylonites, the
636 occurrence of melts at the onset granulite-grade deformation is consistent with the
637 composition of the two ultramylonites shown in Figure 6. Both cases show a clear variation
638 in the neoblastic assemblage crystallized during the strain localization from the proto-

639 mylonite to the ultramylonite zone. In particular, although they are hosted in mineralogically
640 different mylonites, both ultramylonites are formed by anorthitic plagioclase (An_{65} to An_{82}),
641 Ti-rich pargasitic amphibole (TiO_2 1.7–3.7 wt.%), and minor clinopyroxene (Mg# 75 to 85).
642 In contrast to the host rocks (oxide gabbro and troctolite), they do not contain olivine, spinel
643 or Ti-Fe oxides (Figs 6; 7). Felsic rocks containing plagioclase and amphibole are often
644 found in abyssal and ophiolitic gabbros as crosscutting veins or discrete bodies associated
645 with oxide-rich gabbros (Dick et al., 2000; Koepke et al., 2004; 2007; Tribuzio et al., 2014;
646 MacLeod et al., 2017). These rocks are interpreted as the product of crystallization of silica-
647 rich melts produced by extreme fractional crystallization of MOR-type basalt and/or partial
648 melting of hydrothermally altered gabbro (see discussion in Tribuzio et al., 2014). Hence,
649 one can argue that the ultramylonites represent the recrystallization of felsic material
650 originally located within the host rock and mylonitized during the deformation event.
651 However, this is at odds with the high anorthite in plagioclase (An_{83} - An_{65}) and Mg# in
652 clinopyroxene and amphibole (Mg# 75–85 and 67–80 respectively) in the ultramylonites. In
653 addition, the composition of the amphibole in the ultramylonite formed from a troctolite
654 progenitor is similar to that of the amphibole in the host rock (Figure 10b). The temperature
655 estimates for the amphibole-plagioclase couples in the ultramylonite furnish very high values
656 ranging from 930 °C and ~1020 °C, comparable to those in the host mylonites (Fig. 14).
657 Based on these data, it is plausible that the ultramylonite layers may represent melt-rich
658 zones developed during the same deformation event as the host granulite-facies mylonites.
659 The peculiar mineralogical and chemical compositions of these layers indicate that the melt
660 had a hybrid composition, i.e., high Mg/Fe and Ca/Na ratios, but rich in silica, incompatible
661 elements and water. The ultramylonite hosted in an oxide-gabbro, has plagioclase showing a
662 strong increase in anorthite component (~82 mol.%) compared to that in the host mylonite
663 (~46 mol.%). The high anorthite is also ascribable to the occurrence of a water-bearing melt
664 during the crystallization of the neoblastic plagioclase (Berndt et al., 2005). Further
665 investigation will shed light on the nature of this hybrid melt and the mechanism that allowed
666 the strain localization to form the ultramylonite.

667 In summary, our data suggest that the granulite facies deformation event recorded by
668 the gabbros occurred shortly after the crystallization of the magmatic phases. This event may
669 have possibly enhanced the expulsion of the liquid from the crystal framework, allowing the
670 formation of oxide-rich seams within the gabbros and/or discrete oxide-rich horizons often
671 associated with high-temperature deformation. A similar process has been proposed by
672 Natland and Dick (2001) to explain the close association of oxide-rich layers and granulite-
673 grade mylonites in gabbros from Hole 735B at Atlantis Bank. We note though that
674 thermometry estimates of the mylonites analyzed by Miranda and John (2010) from Hole
675 735B yielded temperatures $<910^{\circ}\text{C}$ generally lower than those reported in the present study.
676 Nonetheless, the occurrence of high-temperature ultramylonites likely formed in the presence
677 of melt suggests a complex interplay between deformation and melt percolation that has also
678 been proposed for mylonitic rocks drilled at the inside-corner high of the MAR at 23°N
679 (Agar and Lloyd, 1997).

680

681 **5.3 Hydrothermal alteration**

682 Distinctive black hornblende-rich veins locally crosscut the gabbros at high angle to the high-
683 temperature metamorphic foliation of the host rock. These vein-filled fractures represent
684 formation during brittle deformation that is also related to the crystallization of hornblende
685 pseudomorphs after the magmatic clinopyroxene in the host rock, indicating the host gabbros
686 enjoyed migration of hydrous fluids from the vein into the gabbro. This process also accounts
687 for the formation of secondary plagioclase (albitic in composition) crystallizing within
688 microcracks connecting the different amphibole pseudomorphs.

689 Both the vein and clinopyroxene pseudomorph hornblende in the gabbros have
690 appreciable Cl contents (0.1–0.2 wt.%) similar to that in hydrothermal amphiboles in other
691 abyssal gabbros (Coogan et al., 2001; Cortesogno et al., 2004; Tribuzio et al., 2016). This
692 suggests that both amphibole types formed by interaction with water-rich fluids likely derived
693 from seawater (see also Alt and Bach 2006). However, the amphibole from the veins has lower
694 Mg# (70–77) and higher TiO_2 contents (3.0–3.3 wt.%) compared to the coronitic hornblende

695 adjacent to the veins in the gabbro ($Mg\# = 75\text{--}81$; $TiO_2 < 1.5$ wt.%), approaching the Ti and Al
696 of the magmatic pargasite in the troctolites (Fig. 10). The chemical map in Figure 7d shows
697 that the hornblende statically replacing the pyroxene is associated with fine-grained plagioclase
698 having very low anorthite contents (20–25 mol.%) and is typically found in microcracks.
699 Temperature estimates based on plagioclase-amphibole pairs yield amphibolite facies
700 temperatures of ~ 700 °C (Fig. 14). This suggests that the hornblende replacing the
701 clinopyroxene likely formed by interaction of the magmatic phases with seawater-derived
702 fluids (Coogan et al., 2001), which caused the recrystallization of Na-rich plagioclase within
703 cracks and microveins (see also Tribuzio et al., 2016). On the other hand, the high Ti and Al in
704 the hornblende from the veins suggest that magmatic components were likely still present
705 within the fluids forming these veins. This is in agreement with the high temperature (920–970
706 °C) indicated by the plagioclase-amphibole thermometers on a euhedral plagioclase contained
707 in the vein. The occurrence of magmatic components in the hornblende-rich veins was also
708 inferred for the amphibole-rich veins crosscutting gabbro at Atlantis Bank (Alt and Back, 2006)
709 and in the Ligurian ophiolites (Tribuzio et al., 2014) and related to fluids exsolved from highly
710 evolved melts residual from the magmatic differentiation process.

711 In summary, the microtextures and the chemical variability of the amphibole forming
712 the hydrothermal hornblende offer a snapshot to the retrograde evolution of this portion of the
713 lower crust exhumed by a detachment fault. In line with previous studies on abyssal and
714 ophiolitic gabbros, we propose that a magmatic component was still present during the first
715 stages of hydrothermal alteration at the ductile-brittle transition. This stage was followed by
716 further cooling, by the ingress of seawater along cracks and by the static replacement of the
717 magmatic phases by green hornblende and albitic plagioclase.

718

719 **6. CONCLUSIONS**

720 The lower oceanic crust exposed in the 16.5 °N region of the Mid-Atlantic Ridge formed in a
721 detachment fault system characterized by a moderate to low magma supply. Dredge hauls
722 indicate a bimodal composition of the lower crust that is formed by a high proportion of

723 dunites and troctolites associated with evolved gabbro-norites and oxide gabbros, and a lack
724 of intermediate rock types. Using a thermodynamic model, we infer that a similar bimodal
725 distribution of the lower oceanic crust is expected in regions where gabbroic intrusions are
726 scattered within partly serpentinized mantle peridotite. The formation of these “ephemeral”
727 magma chambers within the mantle lithosphere causes a high eruption rate, which in turn
728 allows most of the melt to be erupted after moderate degrees of fractionation. This idea is
729 also consistent with the evidence that small amounts of melt were present at the onset of the
730 high-temperature deformation related to the oceanic detachment. The development of
731 porphyroclastic to mylonitic fabrics occurred at near-solidus conditions (~1000 °C) and was
732 likely associated with the expulsion of interstitial, evolved melts from the crystal matrix.
733 This mechanism enhanced the formation of disconnected oxide-gabbro seams or layers often
734 associated with crystal-plastic fabrics in the host gabbros. The high-temperature deformation
735 was followed by hydrothermal alteration marked by the formation of amphibole-rich veins at
736 high-temperature conditions (~900 °C). This study suggests that the compositional variability
737 of the lower oceanic crust formed at the 16.5 °N region of the Mid-Atlantic Ridge is the
738 consequence of the complex interplay between low melt supply and high-temperature
739 deformation representing the deep expression of the detachment fault.

740

741 **ACKNOWLEDGMENTS**

742 The geochemical data used in this study and the parameters of the model are included as Tables
743 in the Supplementary Material. The data published will be contributed to the Petrological
744 Database (www.earthchem.org/petdb). We thank the captain and crew of the R/V Knorr for
745 their help and enthusiasm during our cruise to the 16.5° core complexes. Deborah Smith served
746 as best chief scientist ever. Hans Schouten and Joe Cann kept HJBD in line and together with
747 Vincent Salters, Ross Parnell-Turner, Fuwu Ji, Dana Yoerger, Camilla Palmiotto, A.
748 Zheleznov, H. L. Bai, and Will Junkin interpreted the geophysical data and described the rock
749 samples on which this paper is based. A.S was financially supported with an InterRidge
750 fellowship and by the *Societa' Italiana di Mineralogia e Petrografia*. HRM acknowledges

751 support from the Wilhelm und Else Heraeus Stiftung. HJBD acknowledges support from the
752 National Science Foundation grants MG&G 1155650 and MG&G 1434452, and discussions
753 and assistance in the laboratory from Ma Qiang. Fuwu Ji, Joe Cann, Deborah Smith, Hans
754 Schouten, and Ross Parnell-Turner assisted in dredging, sample description, and provide the
755 authors with considerable insight into the geologic and geophysical data collected during the
756 Knorr Cruise 210 Leg 5. Comments by E. Rampono, G Ceuleneer and an anonymous reviewer
757 improved the quality of the manuscript.
758

759 **FIGURE CAPTIONS**

760

761 **Figure 1.** Bathymetric map of the Mid-Atlantic Ridge, 16.5 °N area studied by cruise, R/V
762 Knorr, KNR210-5 (Smith et al., 2014). The location of Southern, Central and Northern Core
763 complexes are also indicated.

764

765 **Figure 2. (A)** Location of the dredges collected during the cruise, R/V Knorr, KNR210-5
766 (Smith et al., 2014). Large pie diagrams refer to the dredges where gabbros or peridotites were
767 collected, dredge numbers are indicated. **(B)** Compositional variability of all lithologies and
768 plutonic rocks from Southern, Central (CC) and Northern Core Complexes (NCC).

769

770 **Figure 3.** Photographs of cut hand specimens of six different plutonic rocks recovered by
771 dredging during R/V Knorr cruise 210-5. Some of the samples show high-temperature crystal-
772 plastic deformation with protomylonitic, mylonitic and ultramylonitic fabrics. In one case, the
773 high-temperature deformation fabrics are cross-cut by lower-temperature brittle fractures and
774 amphibole veins. CPF refers to crystal-plastic fabric as defined in the text.

775

776 **Figure 4.** Microphotographs of selected samples. **(A)** Olivine oikocrysts showing rounded
777 grain boundaries against plagioclase in an undeformed troctolite; **(B)** Large clinopyroxene
778 oikocryst including subrounded olivine and plagioclase chadacryst in a troctolite; Ti-pargasitic
779 amphibole in a sheared troctolite (CPF 1) showing interstitial **(C)** and oikocrystic **(D)** habitus;
780 **(E)** Sheared gabbronorite cut by amphibole vein with diffuse boundaries. Clinopyroxene
781 locally shows partial replacement by amphibole (CPF 2); **(F)** Hornblende corona statically
782 replacing clinopyroxene in the vicinity of the amphibole vein in **(E)**. Ol, olivine; Pl,
783 plagioclase; Cpx, clinopyroxene; Ti-Prg, Ti-pargasite; Hbl, hornblende.

784

785 **Figure 5.** Histogram of deformation intensity of plutonic rocks collected during R/V Knorr
786 cruise 210-5 (see text for detail).

787

788 **Figure 6.** Macroscopic occurrence and microphotographs of the amphibole-plagioclase
789 ultramylonites and host mylonites. **(A)** Troctolite showing a gradual increase in deformation
790 intensity from protogranular to mylonite to ultramylonite (UM). **(B)** Scanned thin-section
791 image of the ultramylonite band crosscutting an oxide-gabbro mylonite. Note that the texture
792 and the mineralogical composition of the two ultramylonites are almost identical, although they
793 are developed in highly different magmatic protoliths.

794

795 **Figure 7.** FEG-SEM compositional maps of selected samples. **(A)** Na, Ca and Mg map of a
796 sheared troctolite clearly showing an increase in Na and decrease in Ca in the neoblastic
797 plagioclase compared to the coexisting porphyroclasts. **(B)** Cr, Ca, Mg, S and Ti maps of the
798 troctolite mylonite including a Amp-Pl ultramylonitic band. The maps show a decrease in Ca in
799 plagioclase in the ultramylonite compared to the mylonite and the distribution of Ti-bearing
800 phases (i.e., amphibole) and Cr-bearing phases (i.e., spinel) between the two lithologies. **(C)** Na
801 and Ti map of the oxide-gabbro mylonite including a amphibole-plagioclase ultramylonitic
802 band. The maps show a sharp decrease in Na in plagioclase in the ultramylonite compared to
803 the mylonite and the lack of Ti-Fe oxides in the ultramylonite. **(D)** Detail of a Na, Mg and Fe
804 map of a gabbro crosscut by an amphibole vein. Note that hornblende replacement is
805 widespread in the vicinity of the amphibole vein, and that Na-rich plagioclase is associated
806 with micro-cracks and late fractures.

807

808

809 **Figure 8.** Variations in TiO₂ **(A)** and Cr₂O₃ **(B)** versus Mg/(Mg+Fe²⁺) (mol.%) in
810 clinopyroxenes from the 16.5°N gabbros. Symbols are grouped per rock-type and indicate
811 single spot analyses (core and rim). The composition of clinopyroxenes from gabbros from
812 other lower crustal sections exposed along the Mid-Atlantic Ridge are also depicted (Ross and
813 Elthon, 1993; Nonnotte et al., 2005; Coogan et al., 2002; Suhr et al., 2008; Drouin et al., 2009;
814 Lissenberg and Dick, 2008; Dick et al., 2010).

815

816 **Figure 9.** Covariations in clinopyroxene $Mg/(Mg+Fe^{2+})$ (mol.%) versus $Ca/(Ca+Na)$ (mol.%)
 817 in plagioclase and $Mg/(Mg+Fe^{2+})$ (mol.%) in orthopyroxene coexisting in selected gabbros.
 818 Dashed arrows indicate the chemical variation in clinopyroxene and plagioclase in the
 819 ultramylonite compared to the host oxide-gabbro mylonite. Data are averaged per sample, error
 820 bars represent one standard deviation of the mean value.

821

822 **Figure 10.** Compositions of amphibole from selected gabbros. (A) Variations in alkali (Na+K)
 823 and TiO_2 (wt.%) versus Al^{IV} (apfu) in amphibole from selected gabbros. (B) Same plot as A
 824 including only core analyses of pargasite and brown hornblende. (C) Chlorine (wt.%) versus
 825 Al^{IV} (apfu) in amphibole; detection limit of EPMA analyses is also indicated. (D) Variations in
 826 TiO_2 (wt.%) versus $Mg/(Mg+Fe^{2+})$ (mol.%) in pargasite and brown-hornblende (core analyses).
 827 Each symbol represents a single spot analysis.

828

829 **Figure 11.** (A) Compositional distribution of basalts from Gakkel Ridge (~500 glass analyses);
 830 Mid-Atlantic Ridge 10–35 °N (~1300 glass analyses); East Pacific Rise 9–13 °E and East
 831 Pacific Rise 9–13 °N (~230 glass analyses) and East Pacific Rise 14–20 °N (~1050 glass
 832 analyses). Data compiled from PetDB (Lehnert et al., 2000). (B) Average compositions and
 833 standard deviation of Na_8 (Klein and Langmuir, 1987) versus $Mg/(Mg+Fe)$ of the basalts in
 834 (A). The average full spreading rates of the regions are also indicated (see also Sinton and
 835 Detrick, 1992 and Coogan, 2007).

836

837 **Figure 12.** Visual explanation of the quantitative model. M1 is the primary melt with
 838 $Mg/(Mg+Fe) \sim 72$ and mass 100g. M2 to M13 are melts produced by the model at steps of
 839 $Mg\# \sim 4$. The mass of melt at each step is calculated as indicated by the italic numbers. B1 to
 840 B12 are melt extracted at each step of the model. Their mass is scaled to reproduce the actual
 841 compositional variability of melts erupted at the MAR (10–35°N). G1 to G13 are gabbros
 842 produced by the model, and forming the “cumulate”. T1 to T12 are melts trapped at each step
 843 and subtracted from the total melt mass. T_{tot} is the sum of T1 to T12 and is used to calculate the
 844 proportion of gabbros crystallized from trapped melts (“trapped”). The “Total” lower crust
 845 composition is given by the sum of gabbros crystallized as “cumulate” + “trapped” (see text for
 846 details).

847

848 **Figure 13.** Liquid $Mg/(Mg+Fe)$ (mol.%) compositions versus (A) olivine Fo (black line and
 849 red circles) and clinopyroxene $Mg/(Mg+Fe)$ (blue line and blue circles); (B) mass of gabbros
 850 (%) crystallized at each step of the thermodynamic model at different mass erupted /mass
 851 crystallized ratios (Me/Mc); (C) trapped melt (%) and (D) liquid density calculated at each step
 852 of the crystallization process. (E) Compositional variability of gabbros resulted from the
 853 thermodynamic model. The origin represents the mass of gabbros neglecting eruption, on the x-
 854 axis are depicted the model outcomes for different Me/Mc ratios if melt entrapment is ignored.
 855 The effect of melt entrapment is shown in the pie diagrams displayed vertically. The vertical
 856 displacement of each diagram depends on the total amount of trapped melt, as represented on
 857 the y-axis. The grey dashed line connects model results for different trapped melt compositions
 858 (see text for details). The compositional variability of the gabbros dredged at the MAR 16.5°N
 859 region, and those from the hole U1309 at the Atlantis Massif (Blackman et al., 2011) are also
 860 reported. (F) Compositional variability of the basalts erupted at different Me/Mc ratios
 861 compared to the basalts from the MAR 10–35°N segment.

862

863 **Figure 14.** Temperature estimates calculated using the edenite-richterite amphibole-plagioclase
 864 thermometer (Holland & Blundy, 1994) assuming a pressure of 200 MPa. Mean values and
 865 standard deviations are given for individual textural amphibole-plagioclase types for each
 866 sample.

867

868

869 **REFERENCES**

- 870 Agar, S.M., G.E. Lloyd (1997), Deformation of Fe-Ti oxides in gabbroic shear zones from the
871 MARK area, in: Karson, J.A., Cannat, M., Miller, D.J., Elthon, D. (Eds.), Proceedings of the
872 Ocean Drilling Program, Scientific Results. Ocean Drilling Program, College Station, TX,
873 pp. 123-135.
- 874 Alt, J. C., W. Bach (2006), Oxygen isotope composition of a section of lower oceanic crust,
875 ODP Hole 735B, *Geochem. Geophys. Geosys.*, 7, Q12008. [http://dx.doi.org/10.1029/
876 2006GC001385](http://dx.doi.org/10.1029/2006GC001385).
- 877 Blackman, D. K., B. Ildefonse, B. E. John, Y. Ohara, D. J. Miller, C. J. MacLeod, and
878 Expedition 304/305 Scientists (2006), Oceanic core complex formation, Atlantis Massif,
879 Proceedings of Integrated Ocean Drilling Program, 304/305, 304, 605 pp., Ocean Drill.
880 Program, College Station, Tex., doi:10.2204/iodp.proc.304305.2006.
- 881 Blackman, D.K., Collins, J.A., 2010. Lower crustal variability and the crust/mantle transition at
882 the Atlantis Massif oceanic core complex. *Geophysical Research Letters* 37, 5 pp.
- 883 Blackman DK, Ildefonse B, John BE et al. (2011) Drilling constraints on lithospheric accretion
884 and evolution at Atlantis Massif, Mid-Atlantic Ridge 30°N, *J Geophys Res*, 116,25
- 885 Buck, W. R., L. L. Lavier and A. N. B. Poliakov (2005), Modes of faulting at mid-ocean ridges,
886 *Nature*, 434, 719–723.
- 887 Borghini G., E. Rampono (2007), Postcumulus processes in oceanic-type olivine-rich
888 cumulates: the role of trapped melt crystallization versus melt/rock interaction, *Contrib
889 Mineral Petrol* 154:619–633
- 890 Cann, J. R., D. K. Blackman, D. K. Smith, E. McAllister, B. Janssen, S. Mello, E. Avgerinos,
891 A. R. Pascoe, and J. Escartin (1997), Corrugated slip surfaces formed at North Atlantic
892 ridge-transform intersections, *Nature*, 385, 329–332.
- 893 Cannat, M. (1993), Emplacement of mantle rocks in the seafloor at mid-ocean ridges, *J.
894 Geophys. Res.*, 98, 4163–4172, doi:10.1029/92JB02221.
- 895 Cannat, M., J.F. Casey, J.F. (1995). An Ultramafic Lift at the Mid-Atlantic Ridge: Successive
896 Stages of Magmatism in Serpentinized Peridotites from the 15 degree N Region, in: Vissers,
897 R., Nicolas, A. (Eds.), *Mantle and Lower Crust Exposed in Oceanic Ridges and in*

- 898 Ophiolites. Kluwer, Norwell, Massachusetts, pp. 5-34.
- 899 Cannat, M., Y. Lagabrielle, H. Bougault, J. Casey, N. de Coutures, L. Dmitriev, Y. Fouquet,
900 (1997). Ultramafic and gabbroic exposures at the Mid-Atlantic Ridge: geologic mapping in
901 the 15°N region. *Tectonophysics* 279, 193-213.
- 902 Cannat, M., D. Sauter, V. Mendel, E. Ruellan, K. Okino, J. Escartin, V. Combier, and M. Baala
903 (2006), Modes of seafloor generation at a melt-poor ultraslow-spreading ridge, *Geology*,
904 34(7), 605–608.
- 905 Coogan L (2007), The lower oceanic crust. In: Turekian KK, Holland KD (eds) *Treatise on*
906 *geochemistry*, vol 3.19. Elsevier, Amsterdam, pp 1–45
- 907 Coogan L.A., A.D. Saunders, P.D. Kempton, M.J. Norry (2000), Evidence from oceanic
908 gabbros for porous melt migration within a crystal mush beneath the Mid- Atlantic Ridge,
909 *Geochem Geophys Geosys*, 1(9). doi:10.1029/2000GC000072
- 910 Coogan L. A., R. N. Wilson, K. M. Gillis and C.J., MacLeod (2001), Near-solidus evolution of
911 oceanic gabbros: insights from amphibole geochemistry, *Geochim. Cosmochim. Acta*, 65,
912 4339–4357.
- 913 DeMets, C., R. G. Gordon, and D. F. Argus (2010), Geologically current plate motions,
914 *Geophys. J. Int.*, 181, 1–80.
- 915 Dick, H. J. B., Bryan, W. B. & Thompson, G. (1981). Low-angle faulting and steady-state
916 emplacement of plutonic rocks at ridge-transform intersections. *EOS* 62, 406.
- 917 Dick, H.J.B., J.H. Natland (1996), Late-stage melt evolution and transport in the shallow
918 mantle beneath the East Pacific Rise. *Proceedings of the Integrated Ocean Drilling Program*,
919 147, pp. 103–134.
- 920 Dick H.J.B., J.H. Natland, J.C. Alt, W. Bach, D. Bideau and Expedition Scientists (2000), A
921 long in situ section of the lower ocean crust: results of ODP Leg 176 drilling at the
922 Southwest Indian Ridge, *Earth and Planetary Science Letters*, 179, 31–51.
- 923 Dick, H. J. B., M. A. Tivey, and B. E. Tucholke (2008), Plutonic foundation of a slow-
924 spreading ridge segment: Oceanic core complex at Kane Megamullion, 23300N, 45200W,
925 *Geochem. Geophys. Geosyst.*, 9, Q05014, doi:10.1029/2007GC001645.

- 926 Drouin M., M. Godard, B. Ildefonse, O. Bruguier, C.J. Garrido (2009), Geochemical and
927 petrographic evidence for magmatic impregnation in the oceanic lithosphere at Atlantis
928 Massif, Mid-Atlantic Ridge (IODP Hole U1309D, 30°N), *Chem Geol* 264:71–88
- 929 Drouin, M., B. Ildefonse, M. Godard (2010), A microstructural imprint of melt impregnation in
930 slow-spread lithosphere: olivine-rich troctolites from the Atlantis Massif (Mid-Atlantic
931 Ridge 30°N, IODP Hole U1309D). *Geochem Geophys Geosyst*, 11:Q06003.
932 doi:10.1029/2009GC002995
- 933 Escartin, J., D. K. Smith, J. Cann, H. Schouten, C. H. Langmuir, and S. Escrig (2008), Central
934 role of detachment faults in accretion of slow-spread oceanic lithosphere, *Nature*, 455, 790–
935 794, doi:10.1038/nature07333.
- 936 Gao, Y., J. Hoefs, E. Hellebrand, A. von der Handt, Snow (2007), Trace element zoning in
937 pyroxenes from ODP Hole735B gabbros: diffusive exchange or synkinematic crystal
938 fractionation?, *Contrib Mineral Petrol* 153:429–442
- 939 Ghiorso, M. S., M.M. Hirschmann, P.W Reiners, and V.C.I. Kress (2002). The pMELTS: A
940 revision of MELTS aimed at improving calculation of phase relations and major element
941 partitioning involved in partial melting of the mantle at pressures up to 3 GPa,
942 *Geochemistry, Geophysics, Geosystems* 3, doi:10.1029/2001GC000217.
- 943 Ghiorso, M.S., O., Sack (1995), Chemical mass transfer in magmatic processes, IV, A revised
944 and internally consistent thermodynamic model for the interpolation and extrapolation of
945 liquid-solid equilibria in magmatic systems at elevated temperatures and pressures,
946 *Contribution to Mineralogy and Petrology* 119, 197–212.
- 947 Gillis K.M., J. Snow et al. (2014) Primitive layered gabbros from fast-spreading lower oceanic
948 crust. *Nature*, 505, 204-207.
- 949 Godard, M., Awaji, S., Hansen, H., Hellebrand, E., Brunelli, D., Johnson, K., Yamasaki, T.,
950 Maeda, J., Abratis, M., Christie, D., Kato, Y., Mariet, C., and Rosner (2009), Geochemistry
951 of a long in-situ section of intrusive slow-spread oceanic lithosphere: results from IODP Site
952 U1309 (Atlantis Massif, 30°N Mid-Atlantic-Ridge), *Earth and Planetary Science Letters*,
953 279, 110–122.

- 954 Hansen, L.N., M.J. Cheadle, B.E. John, S.M. Swapp, H.J.B. Dick, B.E. Tucholke and M.A.
955 Tivey (2013), Mylonitic deformation at the Kane oceanic core complex: implications for the
956 rheological behavior of oceanic detachment faults, *Geochemistry, Geophysics, Geosystems*,
957 14, 3085–3108.
- 958 Holland, T., J. Blundy (1994), Non-ideal interactions in calcic amphiboles and their bearing on
959 amphibole-plagioclase thermometry, *Contrib. Mineral. Petrol.* 116, 433–447.
- 960 Ildefonse, B., D. K. Blackman, B. E. John, Y. Ohara, D. J. Miller, and C. J. MacLeod (2007),
961 Oceanic core complexes and crustal accretion at slow-spreading ridges, *Geology*, 35, 623–
962 626, doi:10.1130/G23531A.1.
- 963 Karson, J. A., Dick H. J. B. (1983). Tectonics of ridge-transform intersections at the Kane
964 Fracture Zone. *Marine Geophysical Researches* 6, 51-98.
- 965 Kinzler R.J., T.L. Grove (1993), Corrections and further discussion of the primary magmas of
966 mid-ocean ridge basalts, 1 and 2, *J Geophys Res*, 98, 22339–22347.
- 967 Klein EM, C.H. Langmuir (1987), Global correlation of ocean ridge basalt chemistry with axial
968 depth and crustal thickness, *J Geophys Res*, 92, 8089–8115
- 969 Koepke J., S. T. Feig, J. Snow and M. Freise (2004), Petrogenesis of oceanic plagiogranites by
970 partial melting of gabbros: an experimental study. *Contrib. Mineral. Petrol*, 146, 414–432.
- 971 Koepke J., Berndt, S.T. Feig and F. Holtz (2007), The formation of SiO₂-rich melts within the
972 deep oceanic crust by hydrous partial melting of gabbros, *Contrib. Mineral. Petrol*, 153, 67–
973 84.
- 974 Lehnert, K., Su, Y., Langmuir, C. H., Sarbas, B. and U. Nohl (2000), A global geochemical
975 database structure for rocks, *Geochemistry, Geophysics, Geosystems* 1,
976 doi:10.1029/1999GC000026.
- 977 Lindsley, D. H., and B. R. Frost (1992), Equilibria among Fe-Ti oxides, pyroxenes, olivine, and
978 quartz: Part I. Theory, *Am. Mineral.*, 77, 987–1003.
- 979 Lissenberg C.J., H.J.B. Dick (2008), Melt–rock reaction in the lower oceanic crust and its
980 implications for the genesis of mid-ocean ridge basalt, *Earth Planet Sci Lett*, 271, 311–325
- 981 Lissenberg C.J., K.A. Howard, C.J. MacLeod, M. Godard (2013), Pervasive reactive melt

- 982 migration through fast-spreading lower oceanic crust (Hess Deep, equatorial Pacific Ocean),
983 *Earth Planet Sci Lett* 361:436–447
- 984 Lissenberg, C. J., C. MacLeod (2016), A reactive porous flow control on Mid-ocean Ridge
985 magmatic evolution, *J Petrol*, 57, 2195–2220
- 986 MacLeod, C. J., R. C. Searle, B. J. Murton, J. F. Casey, C. Mallows, S. C. Unsworth, K. L.
987 Achenbach, and M. Harris (2009), Life cycle of oceanic core complexes, *Earth Planet Sci.*
988 *Lett.*, 287, 333–344.
- 989 MacLeod C.J., H.J.B. Dick, P. Blum, N. Abe, D.K. Blackman (2017), Site U1473. In
990 MacLeod, C.J., Dick, H.J.B., Blum, P., and the Expedition 360 Scientists, Southwest Indian
991 Ridge Lower Crust and Moho, Proceedings of the International Ocean Discovery Program,
992 360: College Station, TX (International Ocean Discovery Program).
- 993 Mehl, L., and G. Hirth (2008), Plagioclase preferred orientation in layered mylonites:
994 Evaluation of flow laws for the lower crust, *J. Geophys. Res.*, 113, B05202,
995 doi:10.1029/2007JB005075.
- 996 Melson W.G., T.L. Vallier, T.L. Wright, G. Byerly and J. Nelson (1976), Chemical diversity of
997 abyssal volcanic glass erupted along Pacific, Atlantic, and Indian Ocean sea-floor spreading
998 centers. In: *The Geophysics of the Pacific Ocean Basin and Its Margin* (AGU, Washington),
999 p 351–367
- 1000 Mendel, V., Sauter, D., Parson, L., Vanney, J. R. (1997). Segmentation and morphotectonic
1001 variations along a super slow-spreading center: The Southwest Indian Ridge (57 degrees E-
1002 70 degrees E). *Marine Geophysical Researches* 19, 505-533.
- 1003 Meyer P.S., H.J.B. Dick, G. Thompson (1989), Cumulate gabbros from the Southwest Indian
1004 Ridge, 548S^78160E: implications for magmatic processes at a slow spreading ridge.
1005 *Contrib Miner Petrol*, 103:44–63
- 1006 Miranda E.A., and B.E. John (2010), Strain localization along the Atlantis Bank oceanic
1007 detachment fault system, Southwest Indian Ridge, *Geochemistry, Geophysics, Geosystems*,
1008 11(4):Q04002.
- 1009 Morse SA (1979), Kiglapait geochemistry II. Petrography, *J Petrol*, 20, 591-624

- 1010 Natland, J.H. and H.J.B. Dick (2001), Formation of the lower ocean crust and the
1011 crystallization of gabbroic cumulates at a very slowly spreading ridge. *Journal of*
1012 *Volcanology and Geothermal Research*, 110, 191–233.
- 1013 Nonnotte P., Ceuleneer G. and Benoit M. (2005) Genesis of andesitic-boninitic magmas at mid-
1014 ocean ridges by melting of hydrated peridotites : geochemical evidence from DSDP Site 334
1015 gabbro-norites. *Earth Planet. Sci. Lett.*, 236, 632-653.
- 1016 Olive, J.-A., M. D. Behn, and B. E. Tucholke (2010), The structure of oceanic core complexes
1017 controlled by the depth distribution of magma emplacement, *Nat. Geosci.*, 3, 491–495,
1018 doi:10.1038/ngeo888.
- 1019 Parnell-Turner, R., H. Schouten, D.K. Smith, (2016), Tectonic structure of the Mid-Atlantic
1020 Ridge near 16°30'N. *Geochem. Geophys. Geosyst.* <https://doi.org/10.1002/2016GC006514>.
- 1021
- 1022 Parnell-Turner, R., J. Escartin, J.A. Olive, D.K. Smith, S. Petersen (2018) Genesis of
1023 corrugated fault surfaces by strain localization recorded at oceanic detachments, *Earth and*
1024 *Planetary Science Letters*, 498, 116–128.
- 1025 Rampone E., G. Borghini, M. Godard, B. Ildefonse, L. Crispini and P. Fumagalli (2016)
1026 Melt/rock reaction at oceanic peridotite/ gabbro transition as revealed by trace element
1027 chemistry of olivine. *Geochim. Cosmochim. Acta*, 190, 309-331
- 1028 Reston, T. J., and C. R. Ranero (2011), The 3-D geometry of detachment faulting at mid-ocean
1029 ridges, *Geochem. Geophys. Geosyst.*, 12, Q0AG05, doi:10.1029/2011GC003666
- 1030 Ross K. and Elthon D. (1993). Cumulates from strongly depleted mid-ocean ridge basalts.
1031 *Nature*, 365, 826-829.
- 1032 Sanfilippo A, Tribuzio R (2013) Origin of olivine-rich troctolites from the oceanic lithosphere:
1033 a comparison between the Alpine Jurassic ophiolites and modern slow spreading ridges,
1034 *Ophioliti*, 38, 89–99
- 1035 Sanfilippo A, H.J.B. Dick HJB, Y. Ohara (2013), Melt-rock reaction in the mantle: mantle
1036 troctolites from the Parece Vela ancient back-arc spreading center, *J Petrol*, 54,861–885
- 1037 Sanfilippo A., T. Morishita, H. Kumagai, K. Nakamura, K. Okino, K. Hara, A. Tamura, S. Arai

- 1038 (2015), Hybrid troctolites from Mid-Ocean ridge, inherited mantle in the lower crust, *Lithos*,
1039 232, 124–130
- 1040 Sanfilippo A., H.J.B. Dick, Y. Ohara and M. Tiepolo (2016a) New insights on the origin of
1041 troctolites from the breakaway area of the Godzilla Megamullion (Parece Vela back-arc
1042 basin): The role of melt-mantle interaction on the composition of the lower crust, *Island*
1043 *Arc*, 25, 220-234, DOI: 10.1111/iar.12137
- 1044 Sanfilippo, A., T. Morishita, R. Senda, (2016b). Rhenium-osmium isotope fractionation at the
1045 oceanic crust-mantle boundary. *Geology*, 44, 167-170. DOI: 10.1130/G37428.1
- 1046 Sauter, D., Patriat, P., Rommevaux-Jestin, C., Cannat, M., Briaais, A., Gallieni Shipboard
1047 Scientific Party. (2001). The Southwest Indian Ridge between 49°15'E and 57°E: focused
1048 accretion and magma redistribution. *Earth and Planetary Science Letters* 192, 303-317.
- 1049 Schroeder, T. J., M. Cheadle, H. J. B. Dick, U. Faul, J. F. Casey, and P. B. Kelemen (2007),
1050 Non-volcanic seafloor spreading and corner-flow rotation accommodated by extensional
1051 faulting at 15°N on the Mid Atlantic Ridge: A structural synthesis of ODP Leg 209,
1052 *Geochem. Geophys. Geosyst.*, 8, Q06015, doi:10.1029/2006GC001567.
- 1053 Sinton, J. M. and R.S. Detrick, (1992), Mid-Ocean Ridge magma chambers, *Journal of*
1054 *Geophysical Research* 97, 197-216.
- 1055 Smith, D. K., J. Escartin, M. Cannat, M. Tolstoy, C.G. Fox, D. Bohnenstiehl, and S. Bazin
1056 (2003), Spatial and temporal distribution of seismicity along the northern Mid-Atlantic
1057 Ridge (15°N to 23.5°N), *J. Geophys. Res.*, 108(B3), 2167, doi:10.1029/2002JB001964.
- 1058 Smith, D. K., J. R. Cann, and J. Escartin (2006), Widespread active detachment faulting and
1059 core complex formation near 13°N on the Mid-Atlantic Ridge, *Nature*, 442, 440–443,
1060 doi:10.1038/nature04950.
- 1061 Smith, D.K., H. Schouten, H.J.B. Dick, J. Cann, V. Salters, H. Marschall, F. Ji, A. Yoerger, A.
1062 Sanfilippo, R. Parnell-Turner, C. Palmiotto, A. Zheleznov, H. Bai, H., W. Junkin, B.M.
1063 Urann, S. Dick, M. Sulanowska, P. Lemmond, S. Curry (2014), Development and evolution
1064 of detachment faulting along 50km of the Mid-Atlantic Ridge near 16.5°N. *Geochem.*
1065 *Geophys. Geosyst.* 15, 4692–4711. <https://doi.org/10.1002/2014GC005563>.

- 1066 Smith, D. K., J. Escartin, H. Schouten, and J. R. Cann (2008), Fault rotation and core complex
1067 formation: Significant processes in seafloor formation at slow-spreading mid-ocean ridges
1068 (Mid-Atlantic Ridge, 13–25°N), *Geochem. Geophys. Geosyst.*, 9, Q03003,
1069 doi:10.1029/2007GC001699.
- 1070 Standish, J. J., Dick, H. J. B., Michael, P. J., Melson, W. G., O'Hearn, T. (2008), MORB
1071 generation beneath the ultraslow-spreading Southwest Indian Ridge (9°-25°E): Major
1072 element chemistry and the importance of process versus source. *Geochemistry, Geophysics,*
1073 *Geosystems* 9, 39 p.
- 1074 Stolper E. and D. Walker (1980), Melt Density and the Average Composition of Basalt,
1075 *Contrib. Mineral. Petrol.* 74, 7-12
- 1076 Tribuzio R., M. Tiepolo and M.F. Thirlwall (2000), Origin of titanian pargasite in gabbroic
1077 rocks from the Northern Apennine ophiolites (Italy): insights into the late-magmatic
1078 evolution of a MOR-type intrusive sequence, *Earth and Planetary Science Letters*, 176, 281–
1079 293.
- 1080 Tribuzio R., M.M. Renna, L. Dallai and A. Zanetti (2014), The magmatic–hydrothermal
1081 transition in the lower oceanic crust: Clues from the Ligurian ophiolites, Italy, *Geochimica*
1082 *et Cosmochimica Acta* 130, 188-211
- 1083 Tucholke, B. E., Lin, J. & Kleinrock, M. C. (1998), Megamullions and mullion structure
1084 defining oceanic metamorphic core complexes on the mid-Atlantic ridge. *Journal of*
1085 *Geophysical Research-Solid Earth* 103, 9857-9866.
- 1086 Tucholke, B. E., M. D. Behn, W. R. Buck and J. Lin (2008), Role of melt supply in oceanic
1087 detachment faulting and formation of megamullions, *Geology*, 36, 455–458.

Figure 1.

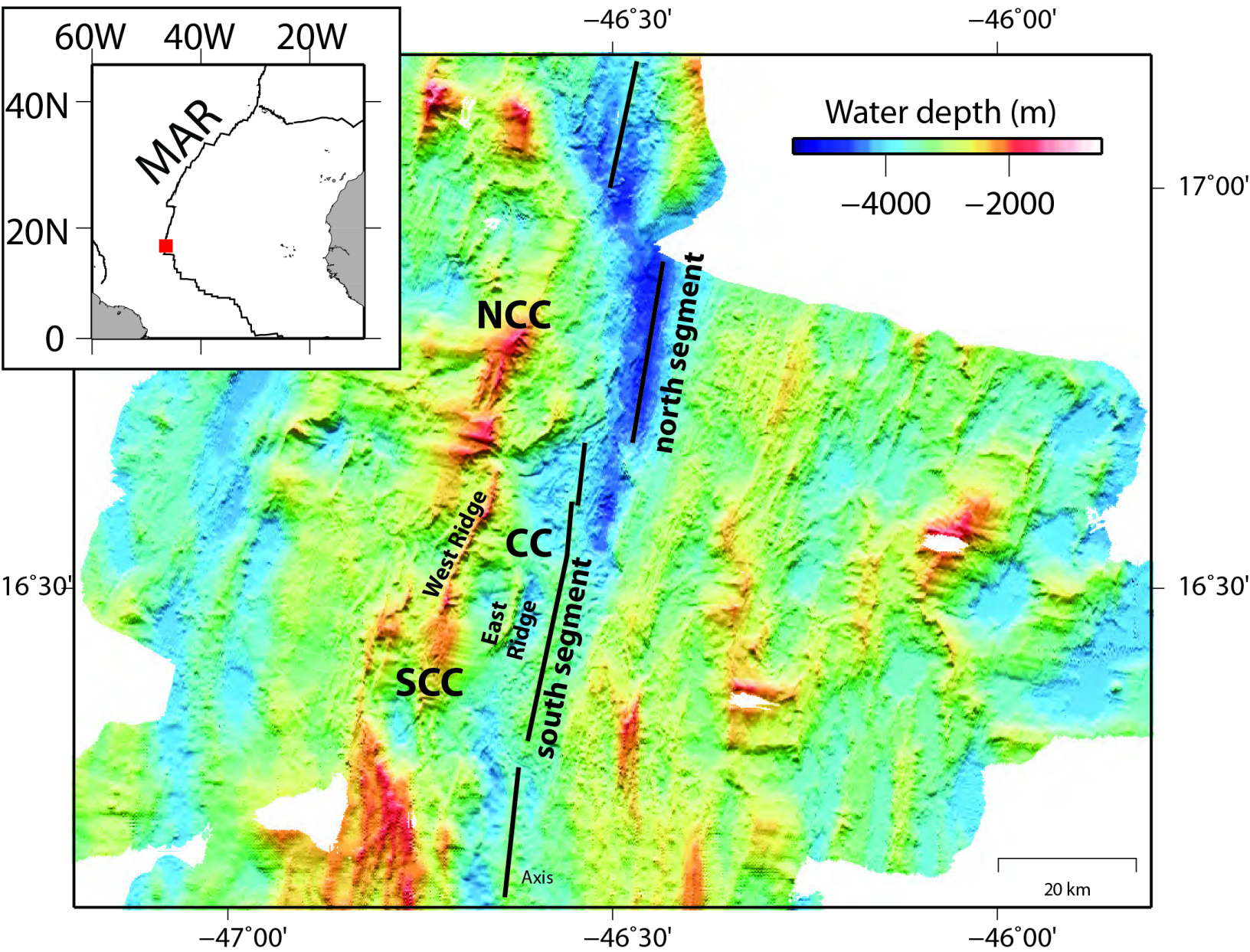
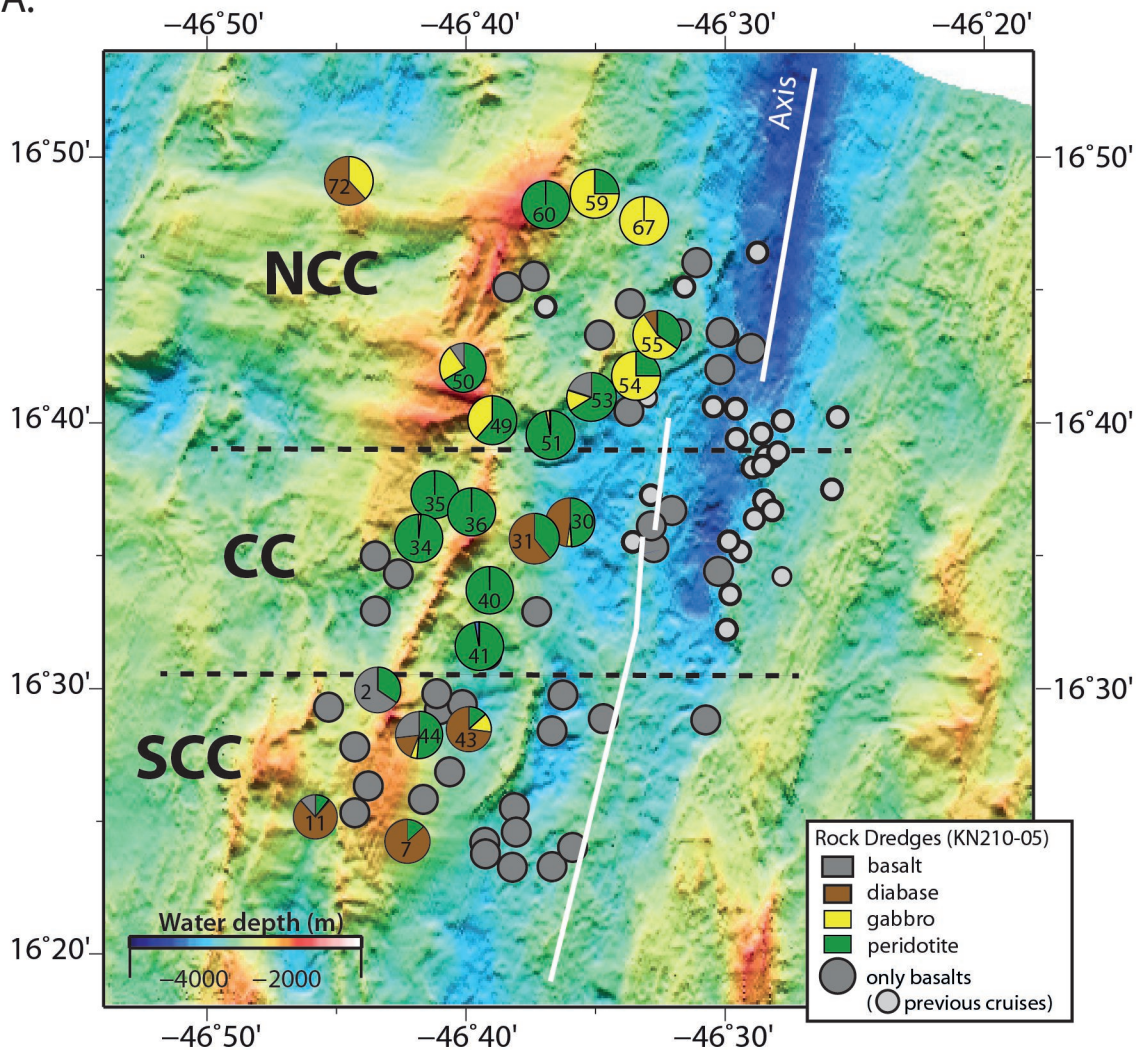


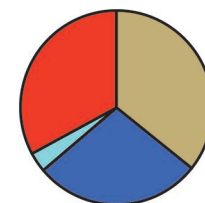
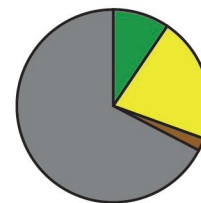
Figure 2.

A.

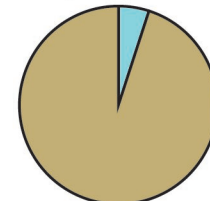
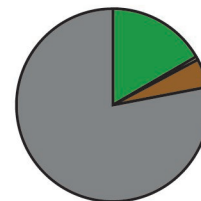


B.

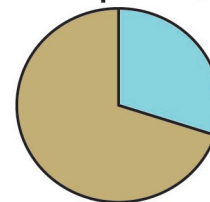
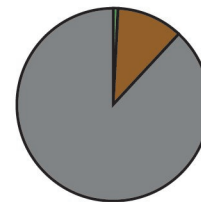
Nothern Core Complex (NCC)



Central Core Complex (CC)



Southern Core Complex (SCC)



Basalt
Diabase
Gabbro
Peridotite

Dunite
Troctolite
Olivine gabbro
Gabbros/norite
Fe-Ti oxide gabbro

Figure 3.

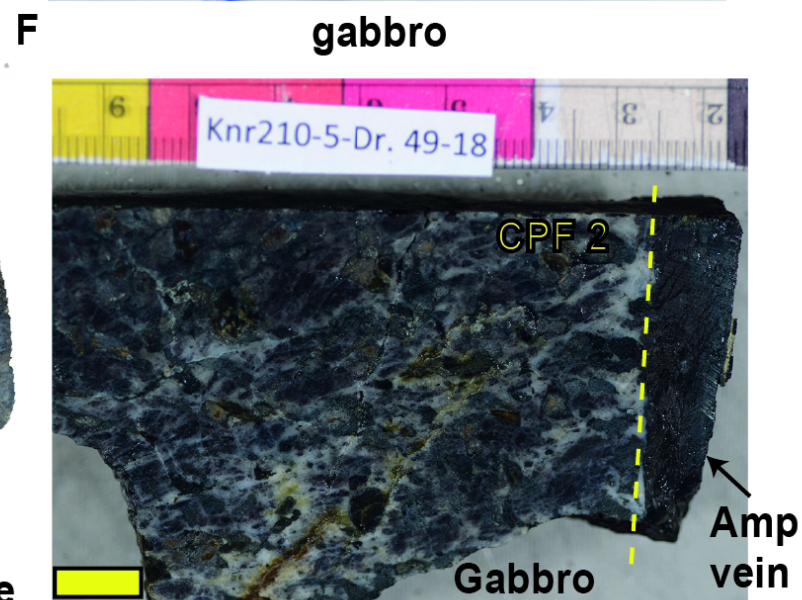
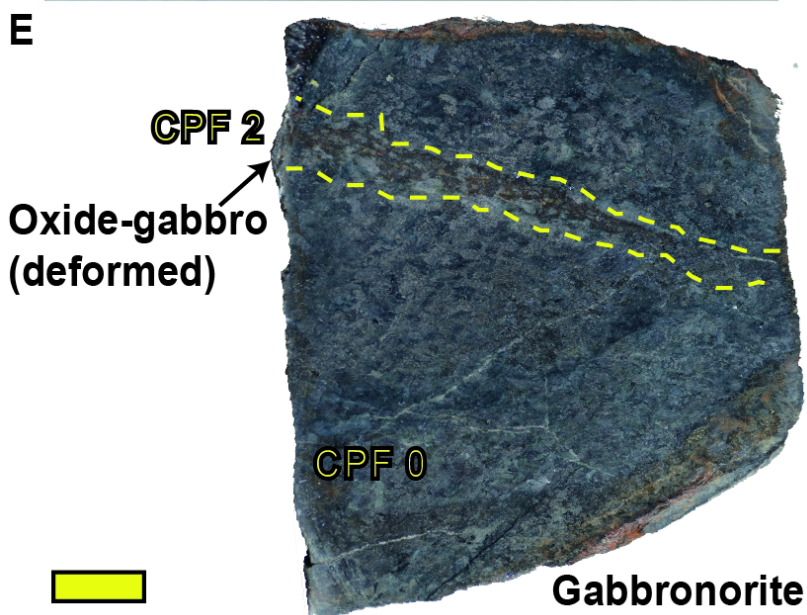
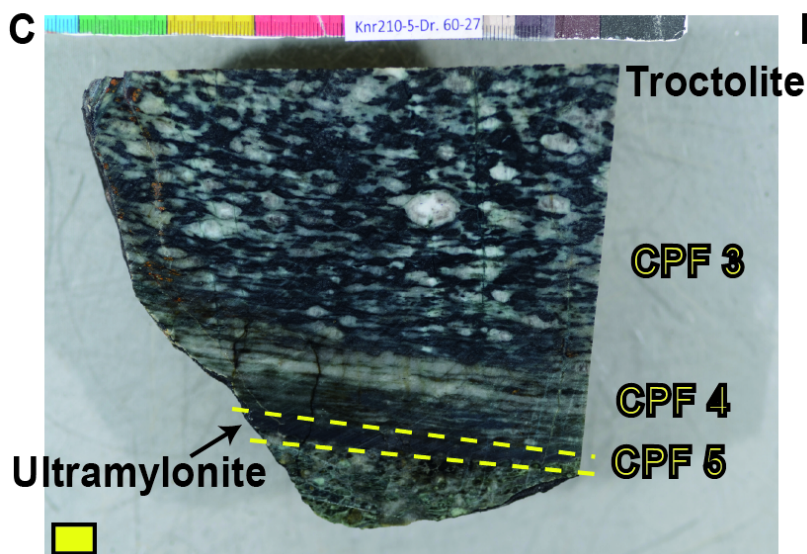
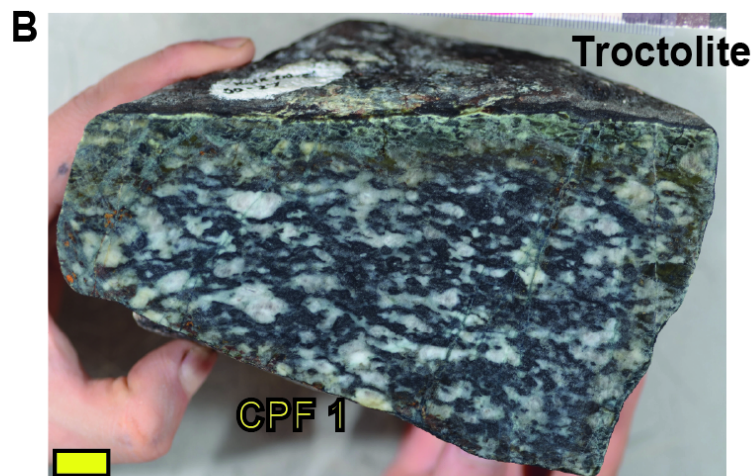


Figure 4.

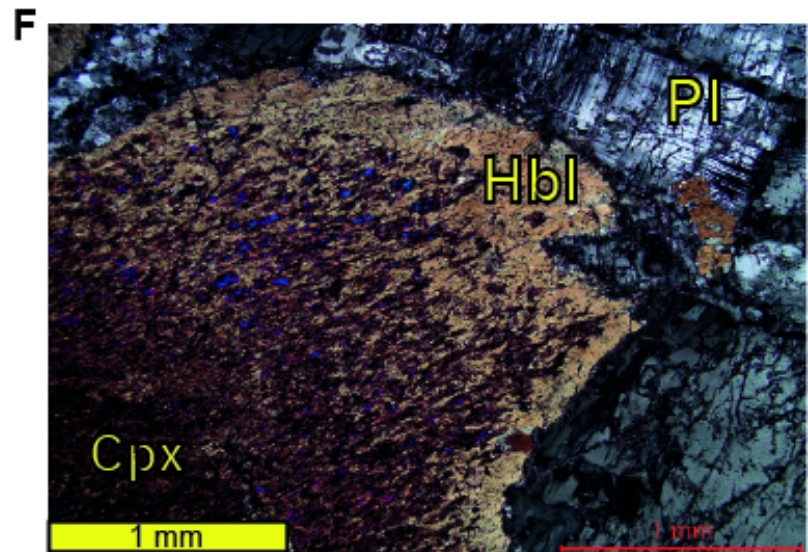
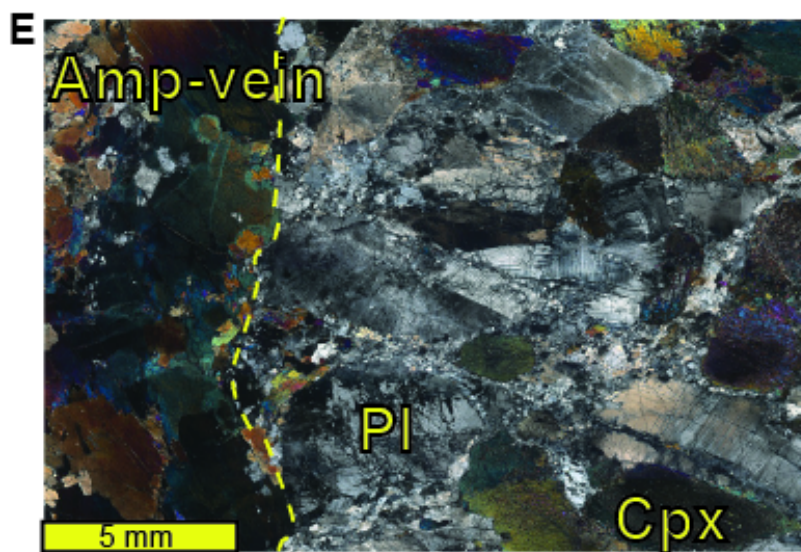
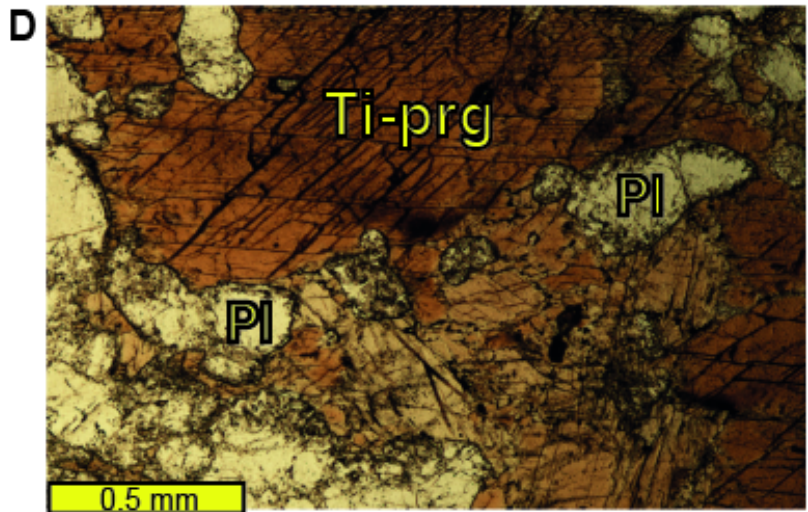
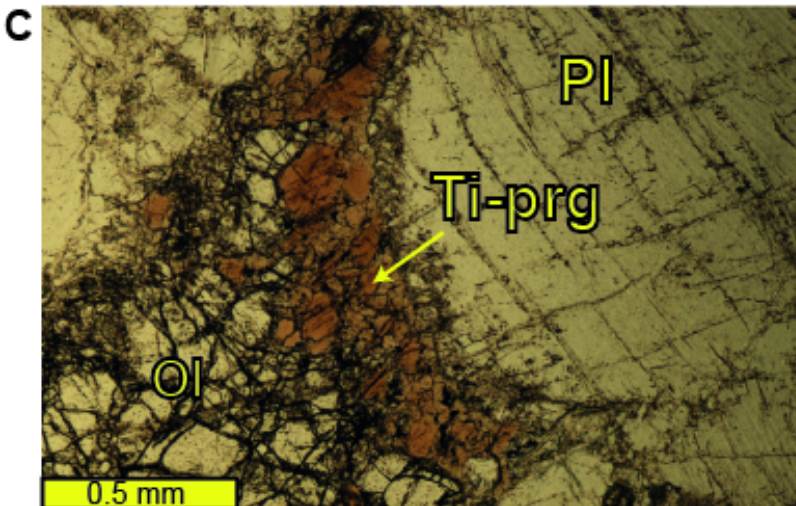
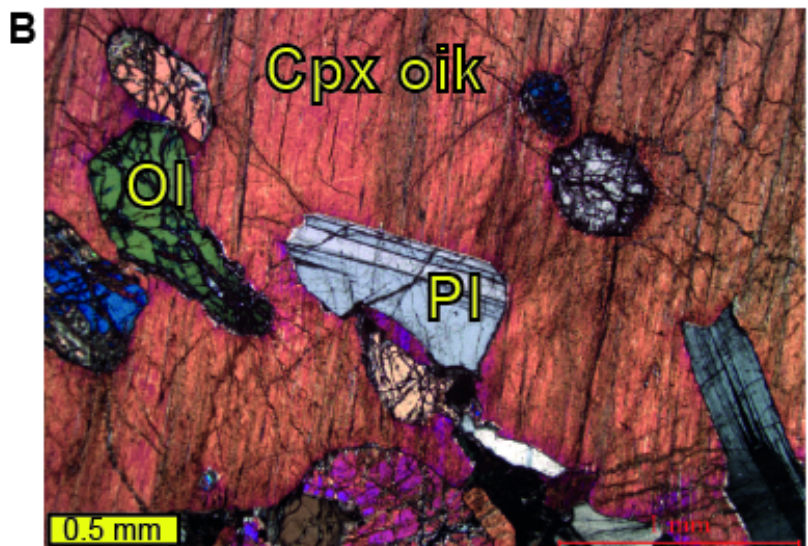
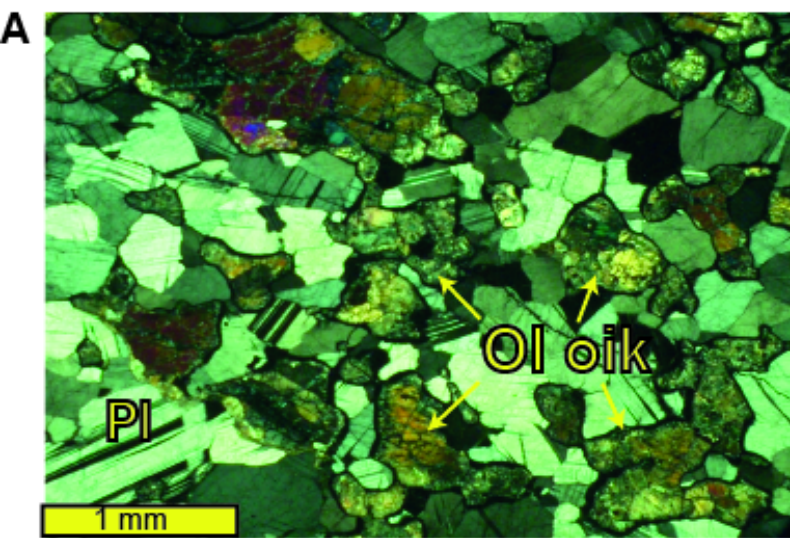
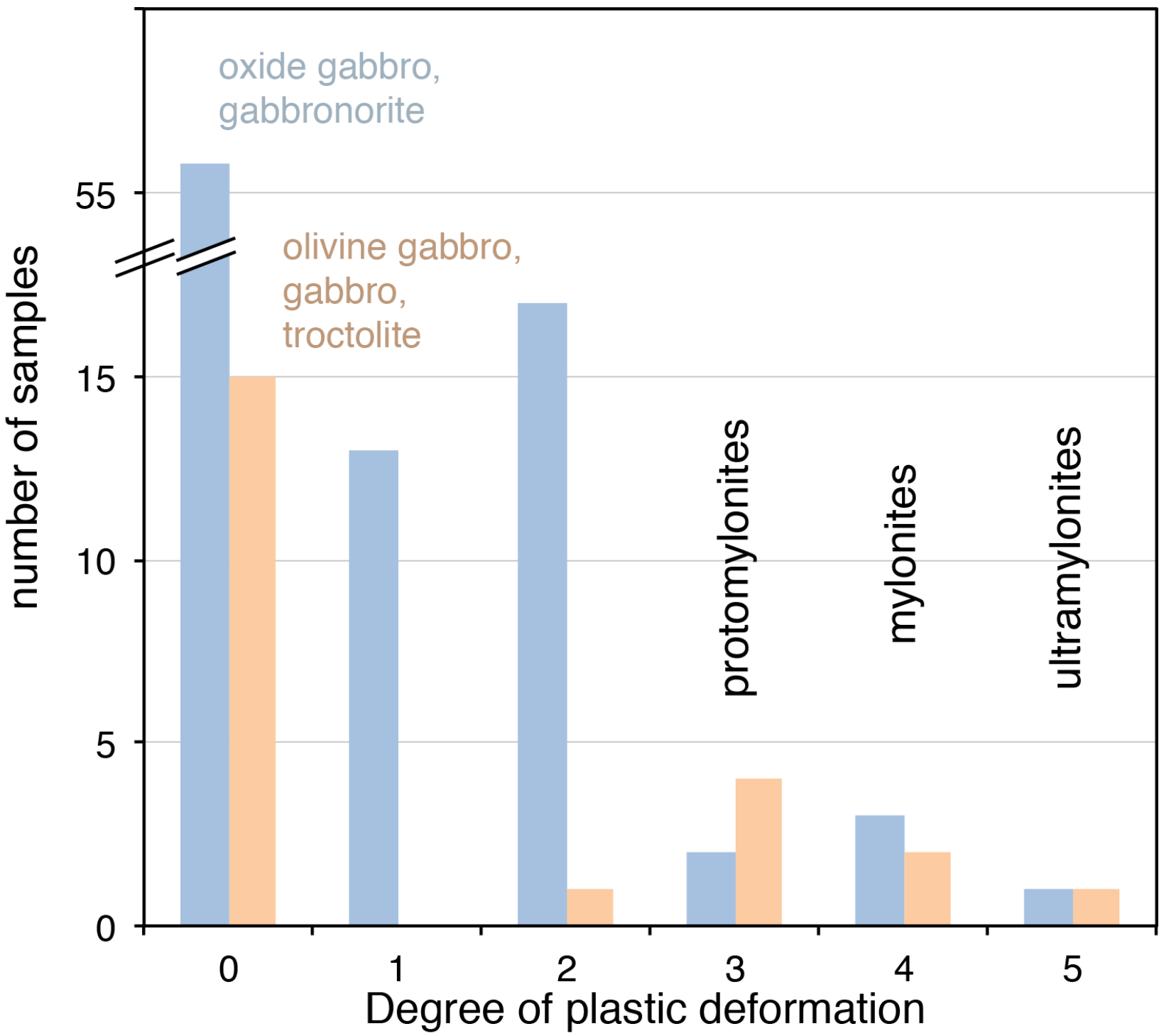


Figure 5.



oxide gabbro,
gabbronorite

olivine gabbro,
gabbro,
troctolite

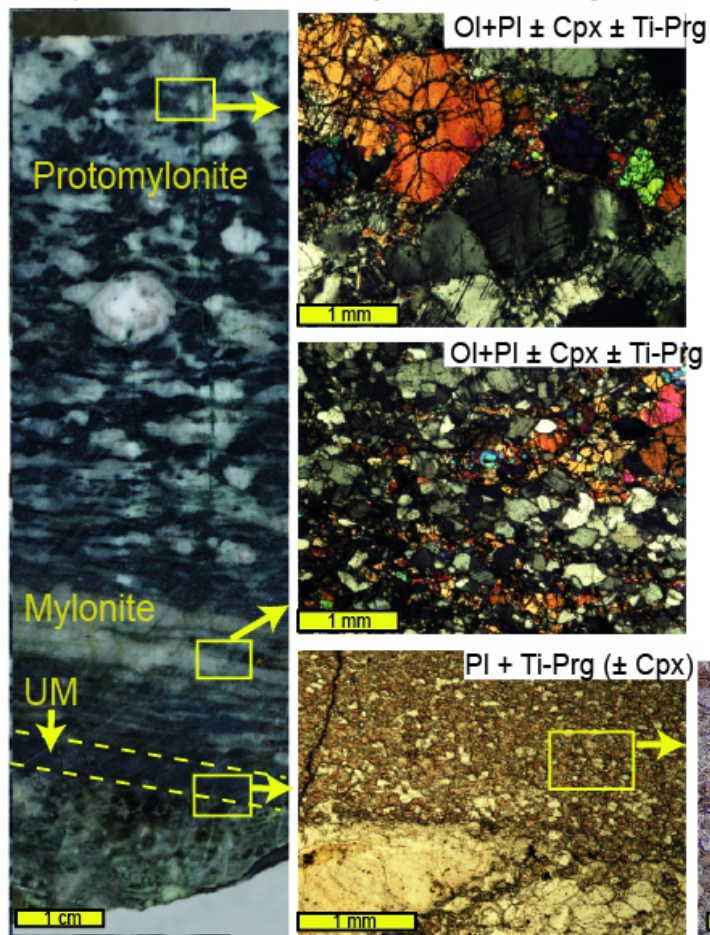
protomylonites

mylonites

ultramylonites

Figure 6.

a) Troctolite / Amp-PI Ultramylonite



b) Ox-gabbro / Amp-PI Ultramylonite

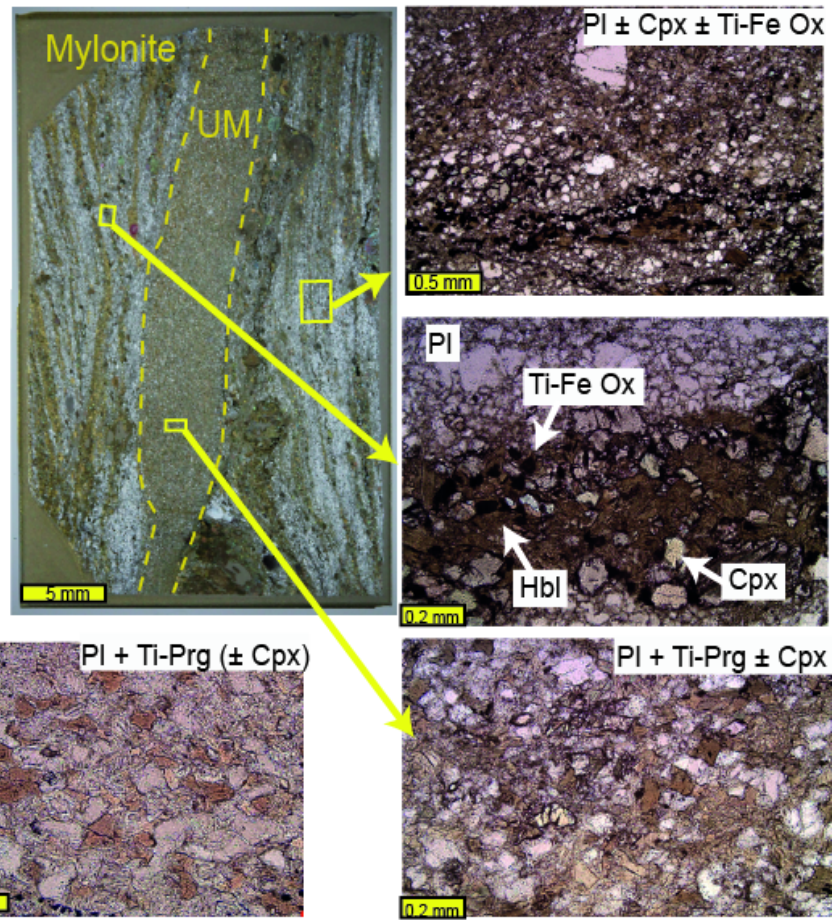
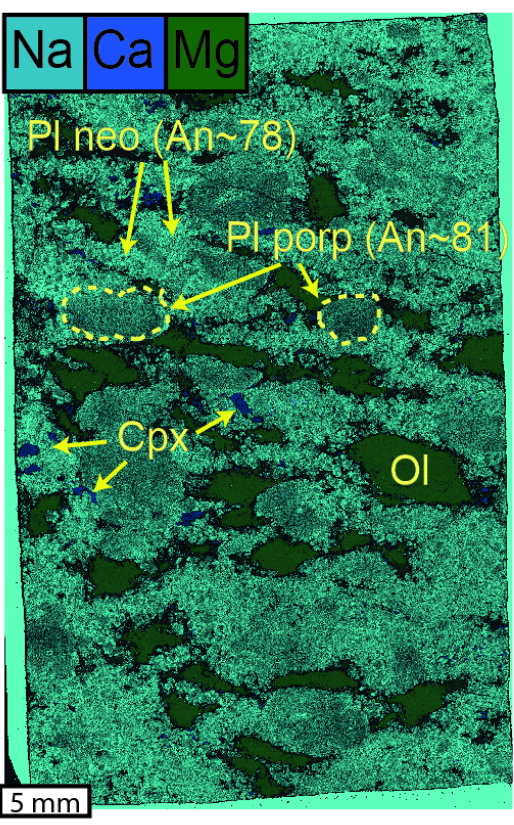
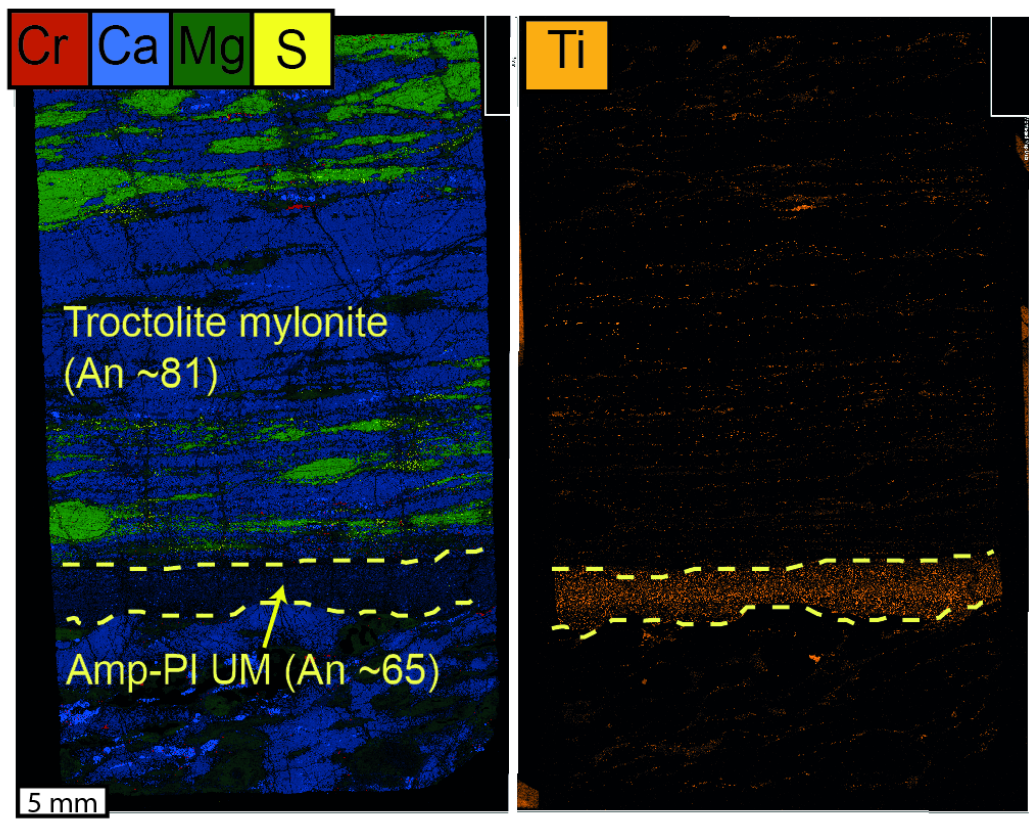


Figure 7.

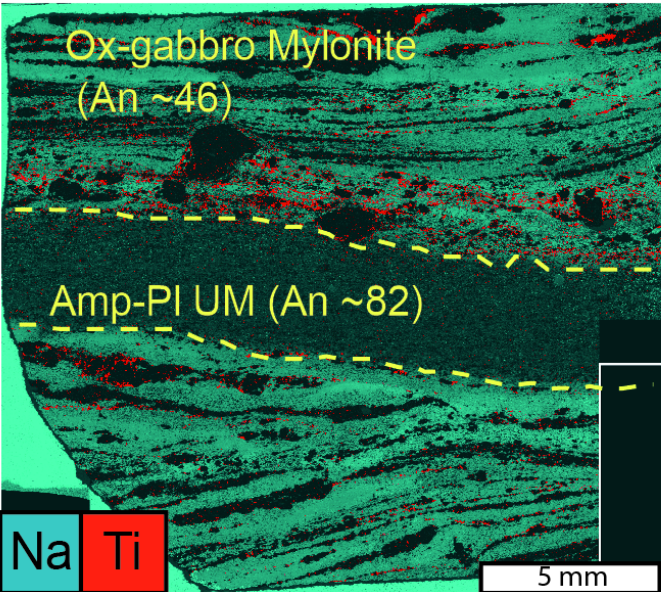
a) Sheared troctolite



b) Troctolite / Amp-PI Ultramylonite



c) Ox-gabbro / Amp-PI Ultramylonite



d) Amp-vein on gabbronorite

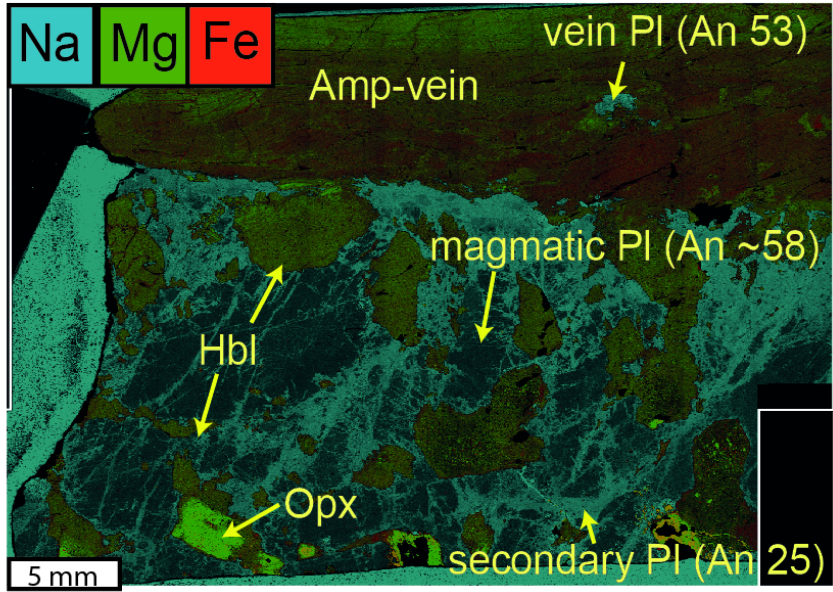


Figure 8.

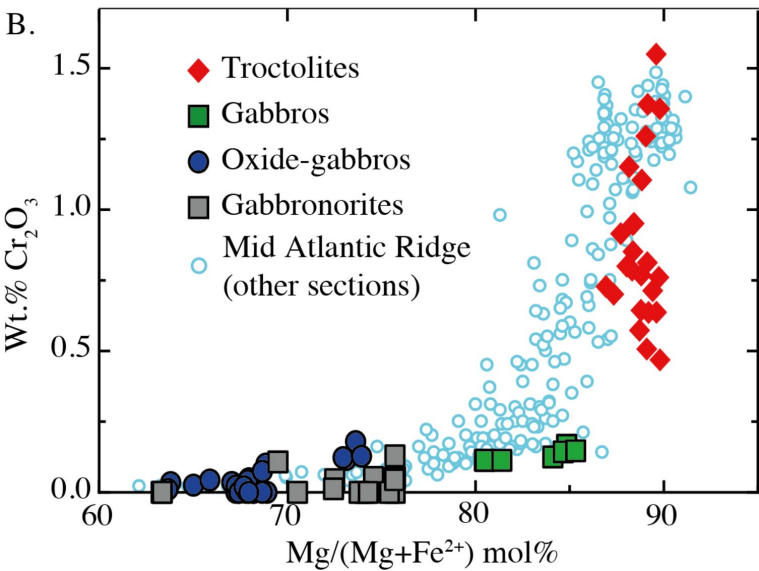
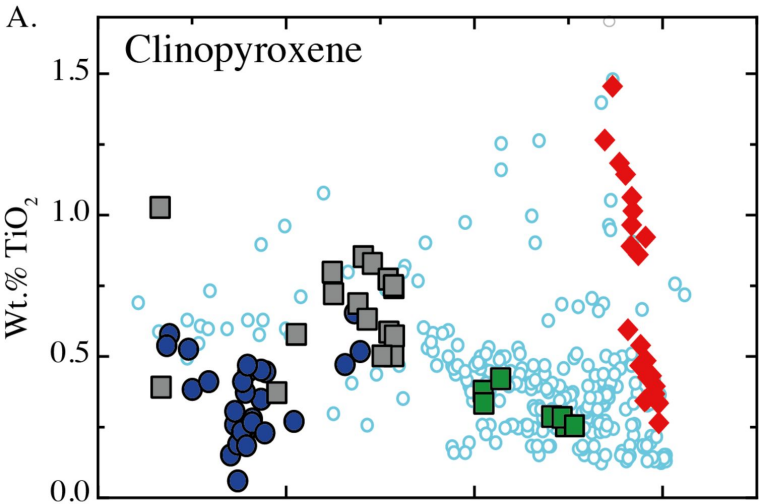


Figure 9.

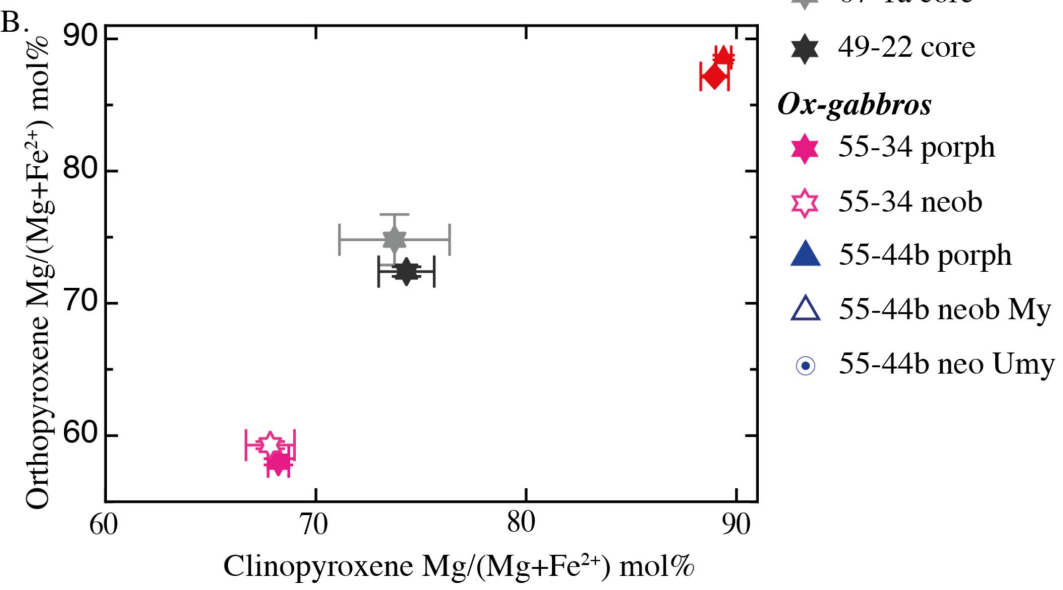
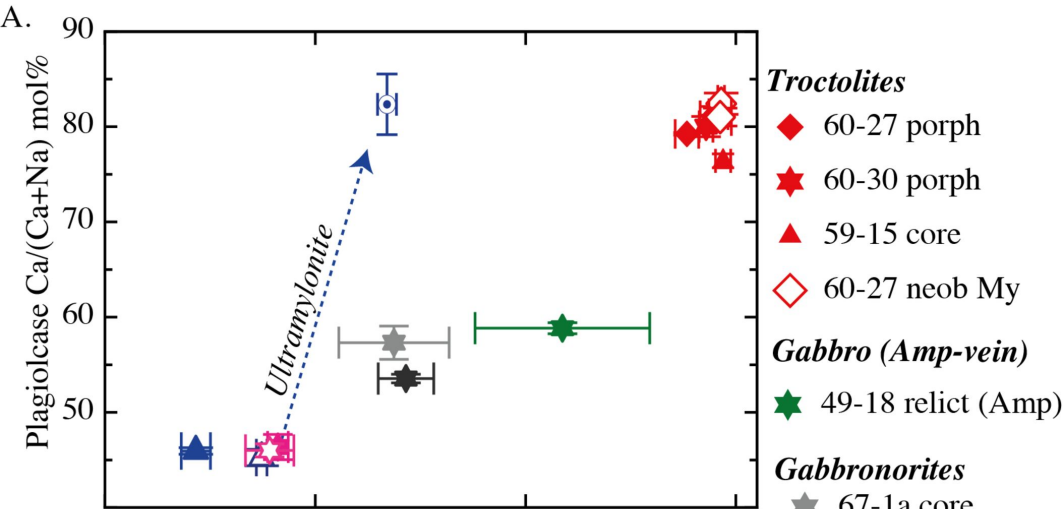
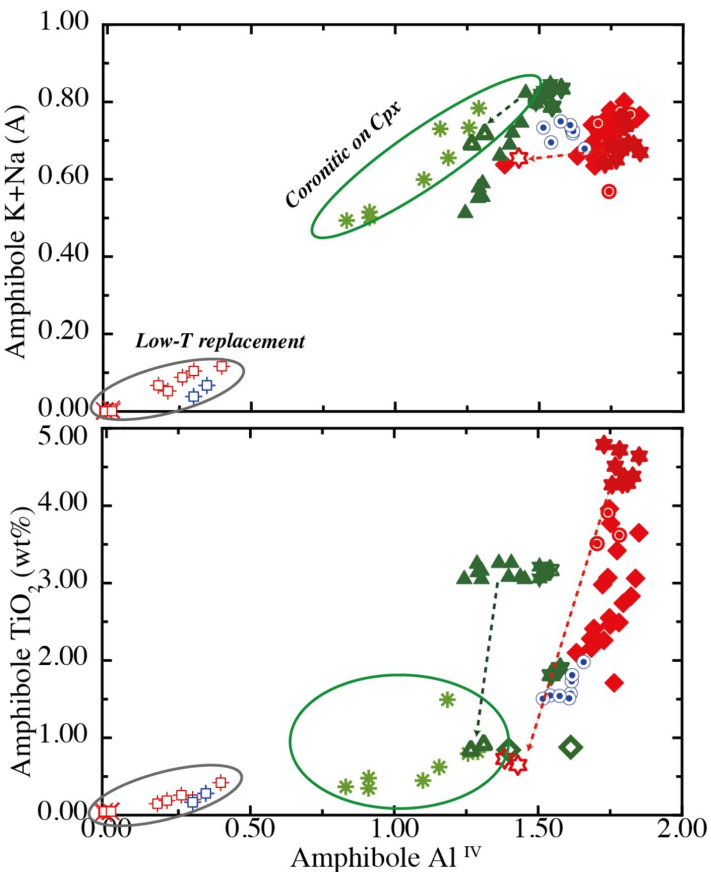
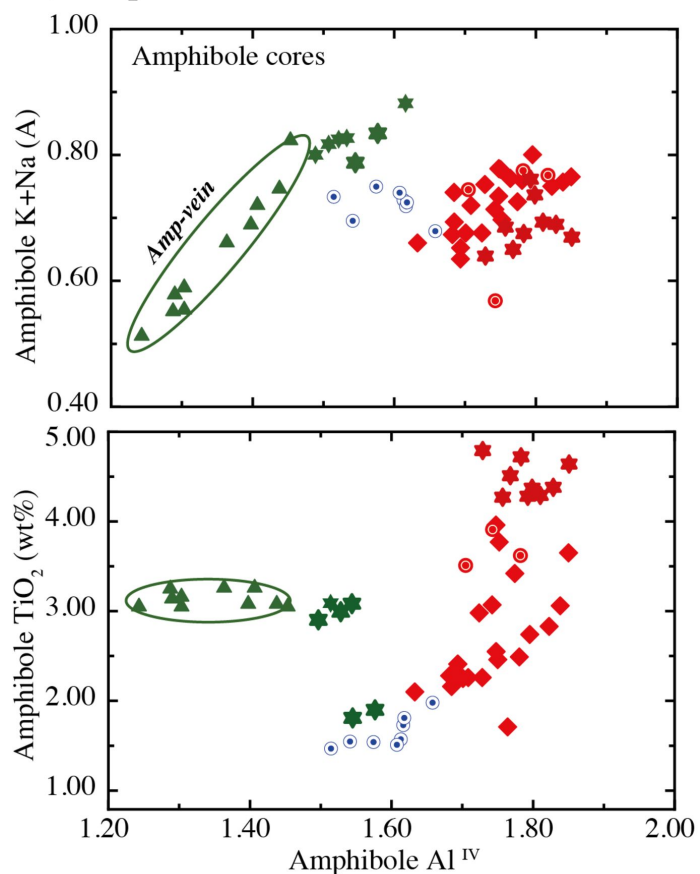


Figure 10.

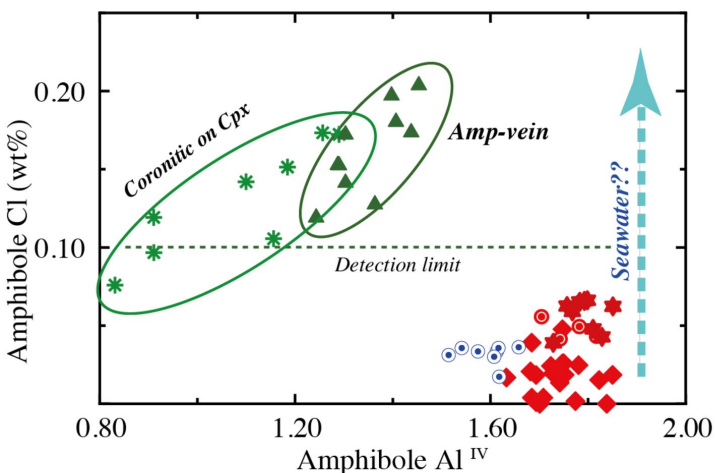
a) All amphiboles



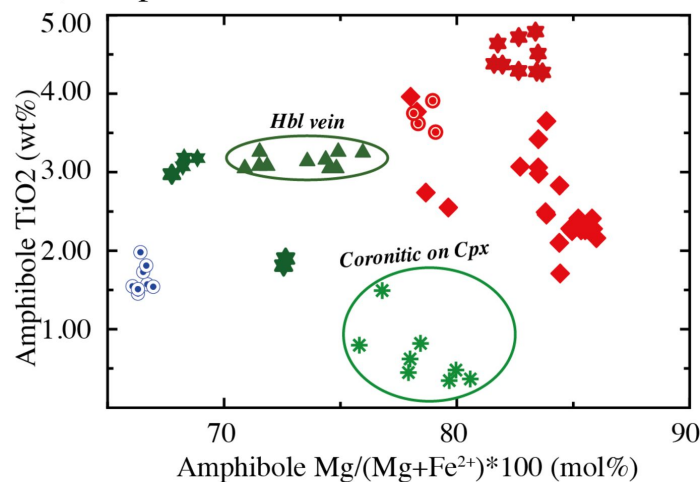
b) Amphibole core



c) Amphibole core



d) Amphibole core

**Troctolites**

- ★ Magmatic core
- ☆ Magmatic rim
- ◆ Neob My
- ⊙ Neob UM

Gabbro (Amp-vein)

- ★ Interstitial
- ▲ Hbl Vein Core
- ▲ Hbl Vein rim
- * Replacing Cpx

Ox-gabbro

- ⊙ Neob UM

Low-T replacement

- ⊠ Replacing Ol (Troct)
- ⊠ Replacing Amp (Troct)
- ⊠ Replacing Amp (Gabbro)

Figure 11.

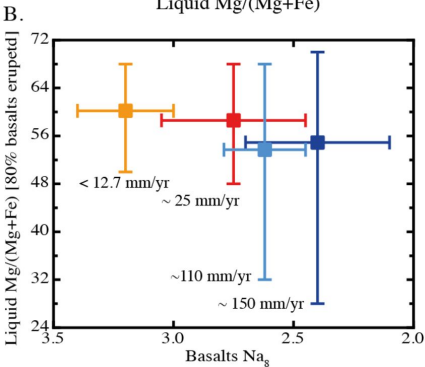
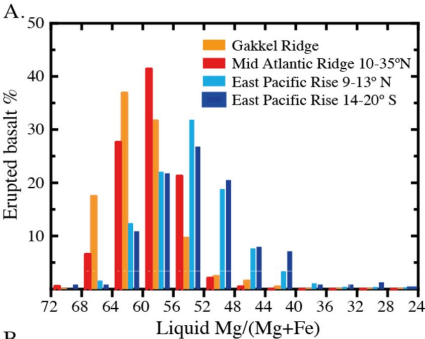
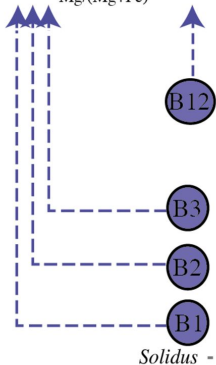
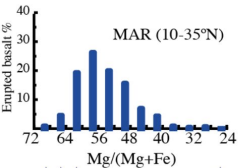


Figure 12.

Basalts



M13 (24)

$$M13 = M12 - G12 - B12 - T12$$

(~5 g)

M4 (60)

$$M4 = M3 - G3 - B3 - T3$$

M3 (64)

$$M3 = M2 - G2 - B2 - T2$$

M2 (68)

$$M2 = M1 - G1 - B1 - T1$$

M1 (72)

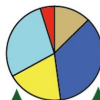
M1(100g)

Lower crust

Cumulate

Trapped

Total



$$T_{tot} = \sum T_{(1-12)}$$

G12

T12

G3

T3

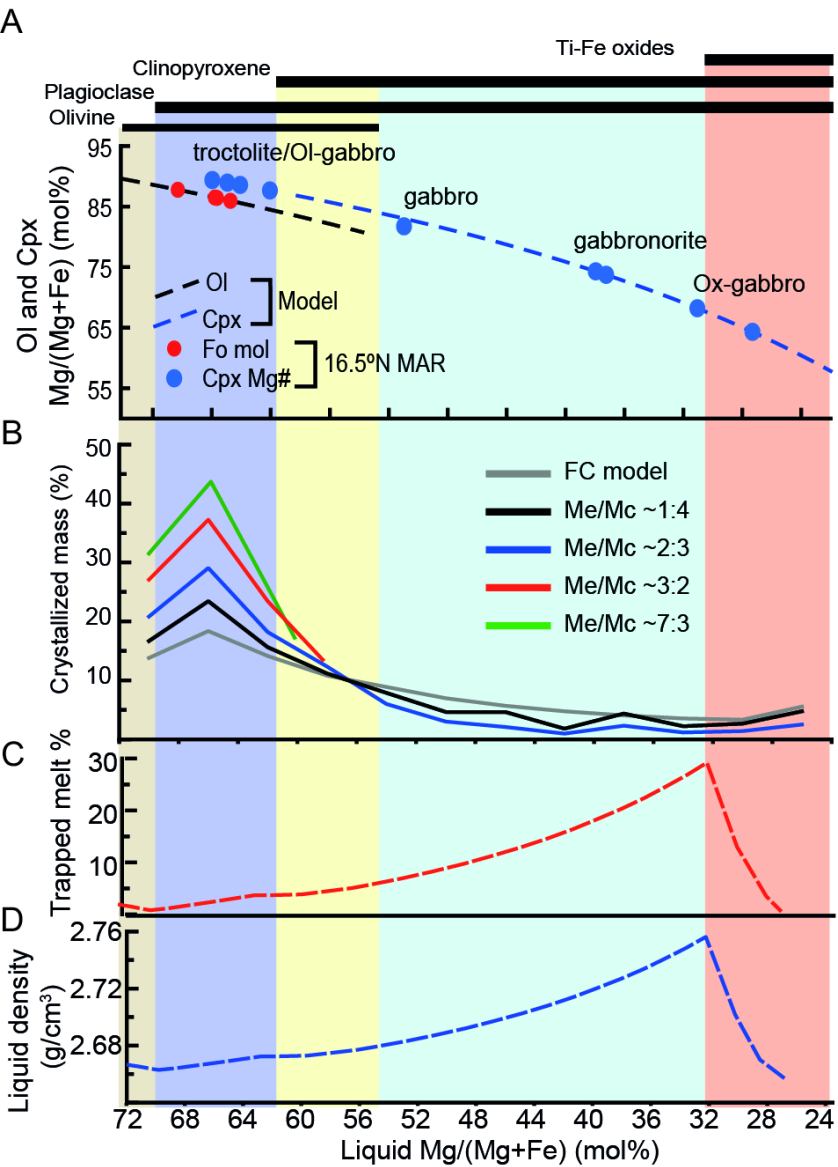
G2

T2

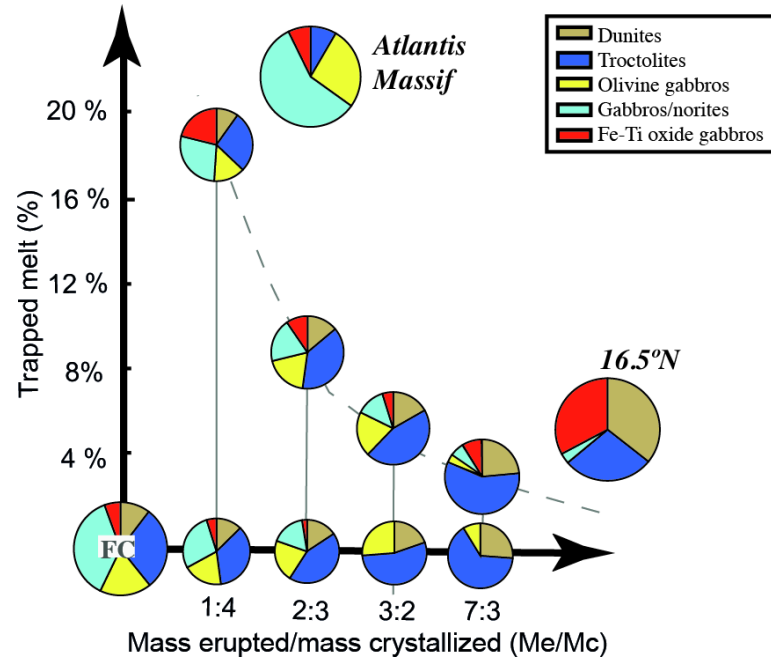
G1

T1

Figure 13.



E Predicted lower crust composition



F Basalt distribution

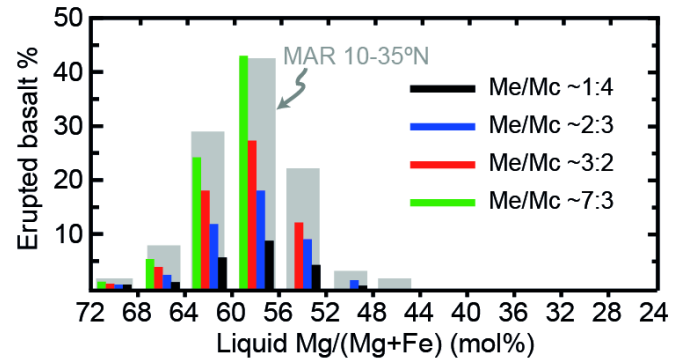


Figure 14.

